REPORT DOCUMENTATION PAGE

Form Approved OMB NO. 0704-0188

The public reporting burden for this collection of information is estimated to average 1 hour per response, including the time for reviewing instructions, searching existing data sources, gathering and maintaining the data needed, and completing and reviewing the collection of information. Send comments regarding this burden estimate or any other aspect of this collection of information, including suggesstions for reducing this burden, to Washington Headquarters Services, Directorate for Information Operations and Reports, 1215 Jefferson Davis Highway, Suite 1204, Arlington VA, 22202-4302. Respondents should be aware that notwithstanding any other provision of law, no person shall be subject to any oenalty for failing to comply with a collection of information if it does not display a currently valid OMB control number.
PLEASE DO NOT RETURN YOUR FORM TO THE ABOVE ADDRESS.

1. REPORT DATE (DD-MM-YYYY)	2. REPORT TYPE	3. DATES COVERED (From - To)
17-08-2015	Ph.D. Dissertation	-

4. TITLE AND SUBTITLE	5a. CONTRACT NUMBER
TERAHERTZ OSCILLATIONS OF HOT ELECTRONS IN GRAPHENE	W911NF-11-1-0434
	5b. GRANT NUMBER
	5c. PROGRAM ELEMENT NUMBER 611102

6. AUTHORS	5d. PROJECT NUMBER
Samwel Sekwao	
	5e. TASK NUMBER
	5f. WORK UNIT NUMBER

7. PERFORMING ORGANIZATION NAMES AND ADDRESSES	8. PERFORMING ORGANIZATION REPORT NUMBER
University of Illinois - Urbana 1901 S. First Street, Suite A Champaign, IL 61820 -7406	

9. SPONSORING/MONITORING AGENCY NAME(S) AND ADDRESS (ES)	10. SPONSOR/MONITOR'S ACRONYM(S) ARO
U.S. Army Research Office P.O. Box 12211 Research Triangle Park, NC 27709-2211	11. SPONSOR/MONITOR'S REPORT NUMBER(S) 58069-EL.11

12. DISTRIBUTION AVAILIBILITY STATEMENT

Approved for public release; distribution is unlimited.

13. SUPPLEMENTARY NOTES

The views, opinions and/or findings contained in this report are those of the author(s) and should not contrued as an official Department of the Army position, policy or decision, unless so designated by other documentation.

14. ABSTRACT

Once a uniform electric field is turned on in graphene, carriers accelerate ballistically until they are scattered by optic phonons and the process repeats itself. In this dissertation, I will show that the oscillatory nature of the motion of the carrier distribution function manifests in damped oscillations of carrier drift velocity and average energy. In appropriate fields, the frequency of such oscillations can be in the terahertz (THz) range. The randomizing nature of optical phonon scattering on graphene's linear band structure further limits terahertz observation to a range of sample lengths.

15. SUBJECT TERMS

Non-linear Transport, Graphene, Terahertz Resonances

16. SECURITY CLASSIFICATION OF:			17. LIMITATION OF ABSTRACT	15. NUMBER OF PAGES	19a. NAME OF RESPONSIBLE PERSON
a. REPORT	b. ABSTRACT	c. THIS PAGE			Jean-Pierre Leburton
UU	UU	UU	UU		19b. TELEPHONE NUMBER 217-333-6813

Standard Form 298 (Rev 8/98)
Prescribed by ANSI Std. Z39.18

Report Title

TERAHERTZ OSCILLATIONS OF HOT ELECTRONS IN GRAPHENE

ABSTRACT

Once a uniform electric field is turned on in graphene, carriers accelerate ballistically until they are scattered by optic phonons and the process repeats itself. In this dissertation, I will show that the oscillatory nature of the motion of the carrier distribution function manifests in damped oscillations of carrier drift velocity and average energy. In appropriate fields, the frequency of such oscillations can be in the terahertz (THz) range. The randomizing nature of optical phonon scattering on graphene's linear band structure further limits terahertz observation to a range of sample lengths.

I will also show that when an ac field is superimposed onto the appropriate dc field, hot carriers in graphene undergo an anomalous parametric resonance. Such resonance occurs at about half the frequency $?F = 2?eF/\sim?OP$, where $2?/?F$ is the time taken for carriers to accelerate ballistically to the optic phonon energy $\sim?OP$ in a dc field F. For weak elastic scattering, the phase difference between the current and the ac field has a nonzero minimum at resonance. Dephasing increases with ac frequency for stronger elastic scattering. The overall effect could also be seen in long-range spatially periodic potentials under steady state conditions.

This dissertation also shows that the soft parametric resonance (SPR) at $? = ??F$ is temperature independent, and the resonance factor $? ? 0.56$ is weakly dependent on the dc field Fo. This ensures tunability of resonant frequencies in the terahertz range by varying Fo. A small signal analysis (SSA) of the time-dependent Boltzmann transport equation (BTE) reveals a second resonance peak at $? ? 1$. This peak is prevalent at temperatures $T ? 77$ K, and appears as a weak shoulder at $T = 300$ K.

Finally, this dissertation shows that in graphene, the motion of carriers under the influence of temporarily and spatially modulated scattering is characterized by sharp resonances. Such resonances occur when the period of the ac field applied equals the time taken by the quasi-ballistic carriers to travel a spatial distance corresponding to the wavelength of the field. I will also show that such scattering can be realized on graphene sheets on periodically spaced gates energized by an a-c bias. Appropriate fields and gate separation will result in high Q-factor resonances in the THz range. The resonant frequencies are tunable with the gate separation, and higher harmonics with large Q-factors can also be achieved.

TERAHERTZ OSCILLATIONS OF HOT ELECTRONS IN GRAPHENE

BY

SAMWEL KEDMON SEKWAO

DISSERTATION

Submitted in partial fulfillment of the requirements
for the degree of Doctor of Philosophy in Physics
in the Graduate College of the
University of Illinois at Urbana-Champaign, 2015

Urbana, Illinois

Doctoral Committee:

      Professor Karen A. Dahmen, Chair
      Professor Jean-Pierre Leburton, Director of Research
      Professor James N. Eckstein
      Associate Professor Timothy J. Stelzer

Abstract

Once a uniform electric field is turned on in graphene, carriers accelerate ballistically until they are scattered by optic phonons and the process repeats itself. In this dissertation, I will show that the oscillatory nature of the motion of the carrier distribution function manifests in damped oscillations of carrier drift velocity and average energy. In appropriate fields, the frequency of such oscillations can be in the terahertz (THz) range. The randomizing nature of optical phonon scattering on graphene's linear band structure further limits terahertz observation to a range of sample lengths.

I will also show that when an ac field is superimposed onto the appropriate dc field, hot carriers in graphene undergo an anomalous parametric resonance. Such resonance occurs at about half the frequency $\omega_F = 2\pi eF/\hbar\omega_{OP}$, where $2\pi/\omega_F$ is the time taken for carriers to accelerate ballistically to the optic phonon energy $\hbar\omega_{OP}$ in a dc field F. For weak elastic scattering, the phase difference between the current and the ac field has a nonzero minimum at resonance. Dephasing increases with ac frequency for stronger elastic scattering. The overall effect could also be seen in long-range spatially periodic potentials under steady state conditions.

This dissertation also shows that the soft parametric resonance (SPR) at $\omega = \eta\omega_F$ is temperature independent, and the resonance factor $\eta \sim 0.56$ is weakly dependent on the dc field F_o. This ensures tunability of resonant frequencies in the terahertz range by varying F_o. A small signal analysis (SSA) of the time-dependent Boltzmann transport equation (BTE) reveals a second resonance peak at $\eta \sim 1$. This peak is prevalent at temperatures $T \leq 77$ K, and appears as a weak shoulder at $T = 300$ K.

Finally, this dissertation shows that in graphene, the motion of carriers under the influence of temporarily and spatially modulated scattering is characterized by sharp resonances. Such resonances occur when the period of the ac field applied equals the time taken by the quasi-ballistic carriers to travel a spatial distance corresponding to the wavelength of the field. I will also show that such scattering can be realized on graphene sheets on periodically spaced gates energized by an a-c bias. Appropriate fields and gate separation will result in high Q-factor resonances in the THz range. The resonant frequencies are tunable with the gate separation, and higher harmonics with large Q-factors can also be achieved.

I would like to dedicate this dissertation to my mother, Nesta Sekwao. Without her guidance, inspiration, and many sacrifices this achievement would not have been possible.

Acknowledgments

I would like to thank my advisor, Professor Jean-Pierre Leburton for his patience, guidance and continuous feedback throughout my time in graduate school. I am grateful for him pushing me to work hard and finally get to this point. Many thanks go to the Physics Department at the University of Illinois for their support during my graduate education. I would also like to acknowledge financial support from the United States Army under the ARO grant W911NF-11-1-0434.

This work would not have been possible without the help of many friends, classmates, and teachers throughout my undergraduate education at the University of Southern Mississippi (USM), and graduate studies at the University of Illinois. I would like to specifically thank my advisor at USM, Professor Lawrence Mead, for his mentorship and inspiring me to pursue a PhD in the subject.

Lastly, but certainly not least, I would like to thank my loving wife and son for their continued patience and support throughout the last years of my graduate studies.

Table of Contents

List of Figures

List of Symbols

H	Hamiltonian
$\hbar$	Reduced Planck's constant $(h/2\pi)$
v_F	Fermi velocity
$\hbar\omega_{OP}$	Optic phonon energy
e	Electronic charge (absolute value)
F	Uniform electric field
τ_{gr}	Expected period of carrier oscillations in graphene
τ_{GaAs}	Oscillation periodicity in gallium arsenide
n_c	Carrier density
k_c	Momentum of carriers with energy $\hbar\omega_{OP}$
τ or τ_{LE}	Low energy relaxation time
E_F	Fermi level
k_F	Momentum of carriers with energy E_F
$S(\vec{k}, \vec{k}')$ or $S_{OP}(\vec{k}, \vec{k}')$	Optic phonon transition rate from a state with momentum $\vec{k}$ to another with momentum $\vec{k}'$
D_o	Optic deformation potential
N_q	Phonon occupation number
σ	Mass density of graphene
A	Area on graphene sheet
$\tau_{OP}(\vec{k})$	Graphene OP scattering time from a state with momentum $\vec{k}$
τ_o	Graphene OP scattering time from a state with momentum $1.5k_c$
E_F	Fermi level
γ	Damping parameter
t^* or τ_F	Approximate time taken by carriers in graphene to complete one cycle
$\tilde{t}$	Dimensionless time
J_x	Current density (x component)

ϵ	Average energy of carriers in graphene (normalized to the initial energy)
ω_F	Frequency of oscillation of carriers in graphene when a uniform electric field F is applied
F_o	DC component of applied field
F_1	AC component of applied field
ω	Frequency of applied ac field
$\Re\{f\}$	Real value of function f
$\Im\{f\}$	Imaginary value of function f
q	Wave number of applied field
λ_F	The average distance travelled by carriers in graphene during one period
Q	Resonance quality factor of carrier oscillations in graphene
THz	Terahertz or 1 x 10^{12} Hz
2D	Two dimensions
3D	Three dimensions
OP	Optic phonon
AP	Acoustic phonon
DF	Carrier distribution function
PR	Parametric resonance
SPR	Soft parametric resonance
BTE	Boltzmann transport equation
LSA	Large signal analysis
SSA	Small signal analysis

Chapter 1

INTRODUCTION

1.1 TERAHERTZ RADIATION

Terahertz (THz) radiation is electromagnetic radiation with frequencies in the range 0.3 - 3 THz.[1] This is a region in the electromagnetic spectrum between the microwave and infrared regions. Because THz waves have wavelengths below 1 mm, they are also referred to as submillimeter waves. This remains the least developed region in the spectrum because of the lack of convenient sources and detectors of THz waves. Consequently, this region of the spectrum is also known as the "terahertz gap".[2] THz waves have attracted a lot of interest in the last two decades because of their wide range of potential applications.[3,4,5,6,7,8] THz radiation could be useful in astrophysics and atmospheric science, biological and medical science, security screening, non-destructive evaluation, communications technology, and ultrafast spectroscopy.[9,10,11]

Terahertz radiation actually occurs naturally as black-body radiation from objects with temperatures grater than 10 K.[12] Even though this thermal emission is very weak for most practical uses, it is still useful in astrophysics.[13] Terahertz waves can also be generated using transistor oscillators and amplifiers, but the output power is too low for most applications. The power generated by such devices falls off at frequencies higher than microwaves as a result of transit-time and resistance-capacitance effects.[14,15] Designing conventional semiconductor diode lasers- that generate infrared and visible radiation-to generate THz radiation has also proved difficult. This is because of the lack of materials with small enough band gaps to generate electromagnetic waves with frequencies below 15 THz.[9]

Significant research efforts has led to the development of some solid-state THz devices.[4] Other sources of THz radiation include THz quantum cascade lasers and resonant tunneling diodes.[9,16,17,18,19] Despite significant improvements in the performance of such devices,[20,1,21] there is still a need for coherent, compact, high-power, and tunable THz sources and detectors that operate at room temperature.

1.2 GRAPHENE

Graphene is a two-dimensional (2D) material with unique electronic properties.[22] Even though the material had been extensively studied many years before,[23] it was not until 2004 that graphene was isolated.[24] This was a remarkable turn of events because it was widely known that strictly 2D materials could not exist.[25,26] The isolation of graphene led to "graphene rush" as the material became the focus of extensive fundamental and technological studies by condensed matter physicists, chemists, and engineers. What really sets graphene apart from conventional semiconductor is that it's electrons behave as massless charged fermions and can be described by a formalism similar to the Dirac relativistic equation rather than the Schröendinger equation.[27] This presents an opportunity to study quantum electrodynamics at the nanoscale level.[28,29] Other exciting properties of graphene include excellent electrical conductivity, optical transparency, mechanical strength, and chemical stability.[30]
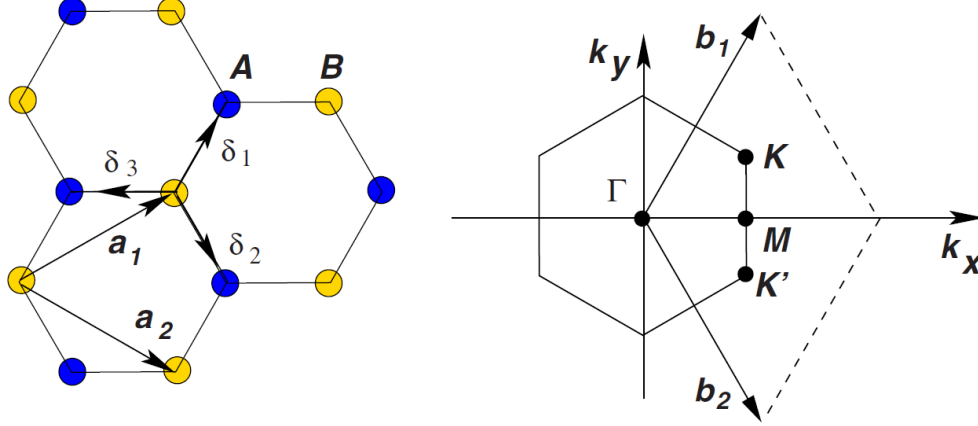
Figure 1.1: (Color online) Left: Graphene lattice with two atoms per unit cell. The vectors $\mathbf{a_1}$ and $\mathbf{a_2}$ are the unit vectors and nearest-neighbor vectors are given by $\delta_i, i = 1, 2, 3$. Right: the corresponding Brillouin zone. The conduction and valence bands in graphene meet at the points K and K' called Dirac points. From Castro Neto, Guinea, Peres, Novoselov, and Geim, *Rev. Mod. Phys.* **81**, 109 (2009). [27]

1.2.1 Graphene Band Structure

Graphene is made up of carbon atoms arranged in a honeycomb structure (Fig. 1.1). Each unit cell of graphene consists of two carbon atoms and is repeated along the lattice vectors $\vec{R} = m\vec{a_1} + n\vec{a_2}$, where

$$\vec{a_1} = a\sqrt{3}(\frac{1}{2}, \frac{\sqrt{3}}{2}), \ \ \vec{a_2} = a\sqrt{3}(\frac{1}{2}, -\frac{\sqrt{3}}{2}) \tag{1.1}$$

and $a \approx 1.42 \mathring{A}$ is the inter-atomic distance. The corresponding Brillouin zone (BZ) has the lattice vectors (Fig. 1.1)

$$\vec{b_1} = \frac{2\pi}{3a}(1, \sqrt{3}), \;\; \vec{b_2} = \frac{2\pi}{3a}(1, -\sqrt{3}). \tag{1.2}$$

The corner points K and K' of the BZ play an important role in the transport properties of graphene. Their locations in momentum space given by

$$\vec{K} = \frac{2\pi}{3a}(1, \frac{1}{\sqrt{3}}), \;\; \vec{K'} = \frac{2\pi}{3a}(1, -\frac{1}{\sqrt{3}}). \tag{1.3}$$

A tight-binding model gives the Hamiltonian of the electrons in graphene as

$$H = -\hbar t \sum_{m,n,\sigma} (a^{\dagger}_{\sigma,m}) b_{\sigma,n} + h.c, \tag{1.4}$$

where $a^{\dagger}_{\sigma,m}(a_{\sigma,m})$ creates (annihilates) an electron with spin $\sigma(\sigma = (+, -))$ on site $\vec{R_m}$ on sublattice A, and $h.c$ is the hermitian conjugate of the first term. The parameter $t \approx 2.8$ eV is the hopping energy between two nearest lattice sites. In the limit of low energies (more relevant for electronic transport), hoppings to next nearest and further neighbours do not play a role and have not been included in Eq. 1.4. The energy bands corresponding to the Hamiltonian (1.4) are given by[23]

$$E(\vec{k}) = \pm \hbar t \sqrt{3 + f(\vec{k})},$$
$$f(\vec{k}) = 2\cos{(\sqrt{3}k_y a)} + 4\cos{\left(\frac{\sqrt{3}}{2}k_y a\right)} \cos{\left(\frac{3}{2}k_x a\right)}, \tag{1.5}$$

where the plus sign is for the upper ($\pi*$) and the minus sign is for the lower (π) band (Fig. 1.2). Note that the two bands meet at six zero energy points called Dirac or neutrality points. By symmetry, these points correspond to the two independent points K and K' in the BZ of graphene.[22,31] Because the two bands touch at the Dirac points, graphene has no band gap, and is referred to as a zero-gap semiconductor. Expanding Eq. 1.5 around $\vec{K}$ or $(\vec{K'})$ we get,[23]

$$E(\vec{k}) \approx \pm \hbar v_F |k| \tag{1.6}$$

for $\vec{k}$ close to $\vec{K}(\vec{K'})$, and $v_F = 3ta/2 \approx 1 \times 10^8$ cm/s. As a result, carriers in graphene travel with Fermi velocity v_F that is much larger than in conventional semiconductors.[32] The high value of v_F and superior conductivity make graphene an attractive material for future high speed electronic devices.[33,34,35,36,37]
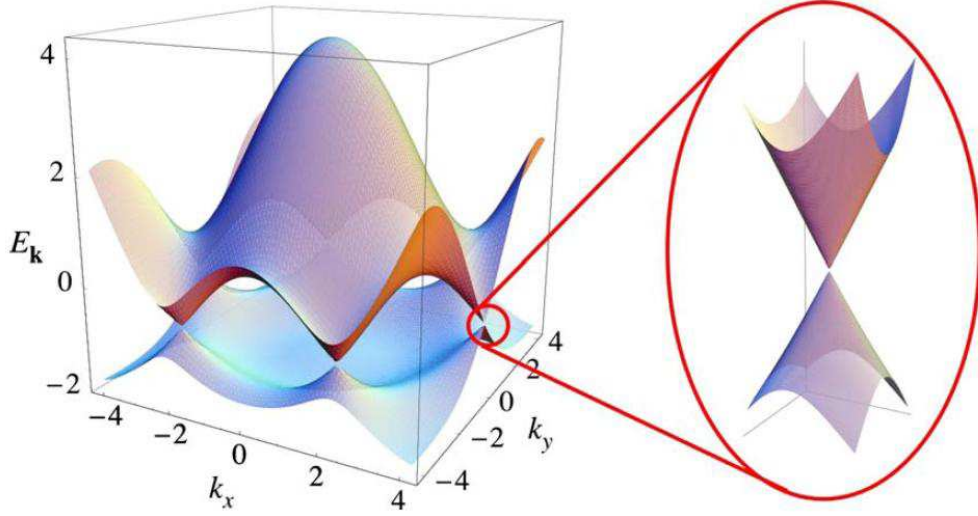
Figure 1.2: (Color online) Graphene band structure. Inset: Band structure close to one of the Dirac points. From Castro Neto, Guinea, Peres, Novoselov, and Geim, *Rev. Mod. Phys.* **81**, 109 (2009). [27]

Because there are two sublattices A and B in the structure of graphene (Fig. 1.1), the Hamiltonian approximates to the Dirac equation

$$H = \hbar v_F \boldsymbol{\sigma} \cdot \boldsymbol{k}, \tag{1.7}$$

where $\boldsymbol{\sigma}$ represents pseudospin due to the two atoms in the unit cell. Thus, electrons in graphene behave like charged relativistic particles that have zero rest-mass and move with speed v_F. As a result, graphene provides a platform to study the physics of massless Dirac fermions in solids.

1.3   OVERVIEW

The main goal of this dissertation is to highlight some of the properties of THz oscillations of hot electrons in graphene. Chapter 2 contains a discussion of dynamics of electrons in the conduction band of graphene, when a a uniform electric field is applied. The chapter also discusses the necessary conditions required to produce room temperature THz oscillations of the electron distribution in graphene.

Chapter 3 includes a study of parametric oscillations of hot carriers in graphene under the influence of an ac field superimposed onto a dc field. Also discussed are the conditions for occurrence of parametric resonance in the THz range, and the tunability of such frequencies with the dc field. Chapter 4 discusses the effects of temperature and the dc field on the THz parametric resonance condition. A discussion on a secondary resonance peak that occurs at low temperatures is also included in the chapter.

The study of electron dynamics in graphene under the influence of spatially and temporary modulated

electric fields is included in chapter 5. Such electric fields and scattering can be realized by placing free standing graphene sheets on periodically spaced gates modulated by an ac field. The chapter discusses the nature of the high Q-factor THz resonances observed, the generation of higher harmonics, and their tunability.

The last chapter discusses the important results of my work and the implications in THz science and technology.

Chapter 2

HOT-ELECTRON TRANSIENT AND TERAHERTZ OSCILLATIONS IN GRAPHENE*

2.1   INTRODUCTION

In graphene, the carrier mean free path for collisions with low energy acoustic phonons (AP) can reach several micrometers, while efficient scattering with monochromatic optic phonons (OP) occurs at much larger energy ($\hbar\omega_{OP} \sim 0.2$ eV).[38,39] Therefore, in electric fields F high enough (to escape AP or low-energy scattering), charge carriers can experience quasiballistic runaway until they scattered with efficient OP emission once $E \geq \hbar\omega_{OP}$.[40] The *coherent* aspect of this process, that is, *the coherent acceleration* of the carrier distribution function followed by quasi-instantenous carrier relaxation by OP's at high energy, is expected to produce oscillations of the carrier velocity with a periodicity given by $\tau_{gr} = \hbar\omega_{OP}/eFv_F \sim 1$ ps (Ref. 41) for $F \sim 2$ kV/cm, that is, in the terahertz range.

This type of oscillation has already been predicted in GaAs,[41] and indirectly observed in slightly n-doped InSb.[42] However, their manifestation in these materials is different in several respects: First, owing to the carrier parabolic energy-momentum dispersion, the oscillation periodicity in GaAs is instead given by $\tau_{GaAs} = \sqrt{2m * \hbar\omega_{OP}^{GaAs}}/eF$.[41,43,44] Second, and more importantly, in III-V semiconductors, the oscillation onset is restricted by two conflicting conditions: On the one hand, the low value of the OP energy ($\hbar\omega_{OP} \sim$ 0.04 eV) (Ref. 45) is comparable to the thermal broadening of the carrier distribution at room temperature so that the back-and-forth motion of the distribution between the optic phonon and the zero point energy is immediately damped.[41,43,44] On the other hand, at low temperature, ionized impurity scattering becomes dominant and produces strong damping which can only be reduced by lowering the dopant density, thereby lowering the carrier density, and weakening the oscillation amplitude. In this respect, the high conductance of graphene, and the high optic phonon energy provide the conditions for room-temperature observation.

This chapter provides a study of carrier dynamics in graphene single layers, once the electric field has been turned on, to determine the conditions of occurrence of current oscillations. Indeed, thermal broadening of the initial distribution introduces a decoherence in the OP relaxation among carriers, which, aside from

*This chapter closely follows Samwel Sekwao, and Jean-Pierre Leburton, *Phys. Rev. B* **83**, 075418 (2011).

low-energy scattering, causes inherent damping of the oscillations, especially at high fields, where carriers overshoot the OP energy before emission. For this purpose, the Boltzmann formalism is used to solve for the steady state and the time-dependent carrier distribution in the presence of OP scattering.[41,43,44] Since both intravalley and intervalley scattering can be treated within the deformation-potential interaction model,[46] an overall transition rate accounting for both mechanisms is used. Low-energy scattering such as impurities and acoustic phonons by are accounted for using the relaxation time approximation,[47] but the dissipation effects due to the environment such as remote phonons,[48] detrimental to the occurrence of the oscillations are ignored, which limits their observations optimally to suspended graphene or nonpolar substrate.[49] In weak concentrations ($n_c \sim 10^{11}$ cm^{-2}), electron-electron interactions do not play a major role in transport in graphene,[27] and they are not included in this analysis. This chapter also analyses the interplay between applied electric fields and strength of the low- energy scattering rates for the onset of oscillations is provided. In particular it is shown that unlike in III-V semiconductors, where the OP polar nature focuses the low-energy repopulation along the field, and provides a "streaming" profile to the carrier distribution, in graphene, the randomizing scattering by deformation potential OP generates of a transient crater-like shape in the low-energy distribution.

2.2   MODEL

Let us consider a system of electrons in the graphene conduction band under the influence of an electric field along the x-direction. The momentum space can be divided into two regions: I ($k < k_c$) and II ($k > k_c$) separated by a circle of critical momentum $k_c = \omega_{OP}/v_F$, which corresponds to the electron kinetic energy equal to $\hbar\omega_{OP}$ [Fig. 2.1(a)]. In region I electrons undergo quasiballistic acceleration and weak scattering by low-energy mechanisms (e.g., impurities or AP's) until they reach region II where they lose their energy by OP emission, and scatter back to region I. In this model, the electric field is assumed to be low enough so that electrons are scattered efficiently from region II to region I by OP emission with little probability to reach $E \geq 2\hbar\omega_{OP}$.

Quite generally, the time-dependent Boltzmann equation in each region can be written as;

$$\frac{\partial f_I(\vec{k},t)}{\partial t} + \frac{eF}{\hbar}\frac{\partial f_I(\vec{k},t)}{\partial k_x} = -\frac{f_I(\vec{k},t) - f_o(\vec{k})}{\tau} + \sum_{\vec{k}'} S(\vec{k}',\vec{k})f_{II}(\vec{k}',t) \tag{2.1a}$$
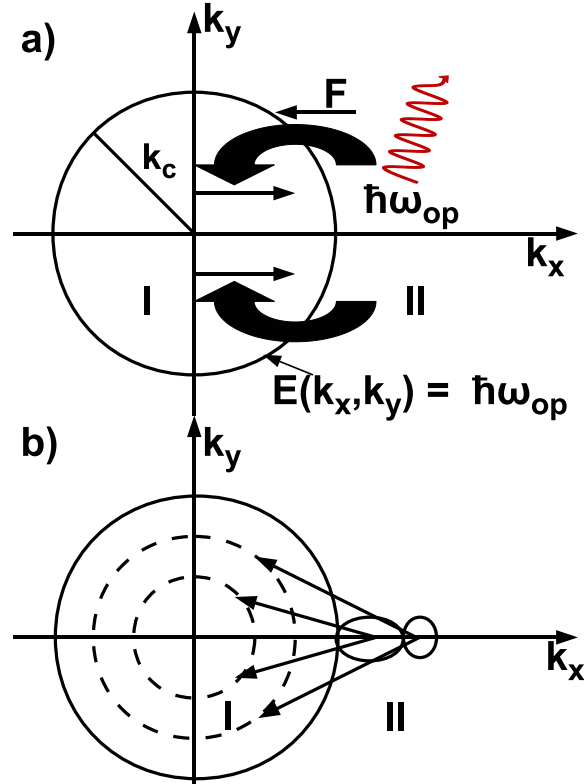
Figure 2.1: (Color online) a) Schematics of carrier quasiballistic acceleration and OP scattering in 2D k space. The solid circle of radius k_c is the locus of all points in k space corresponding to the carrier energy $\hbar\omega_{OP}$. b) Schematics of electrons scattered by OP's from two different positions of the distribution function shown by ovals in region II. The dashed circles in region I represent the two areas of high momentum probability where electrons are more likely to land after OP emission from the distribution in region II at two different times. The arrows represent the electron transitions from II to I.

$$\frac{\partial f_{II}(\vec{k},t)}{\partial t} + \frac{eF}{\hbar}\frac{\partial f_{II}(\vec{k},t)}{\partial k_x} = -f_{II}(\vec{k},t)\sum_{\vec{k}'}S(\vec{k},\vec{k}') \qquad (2.1b)$$

where $f_I(\vec{k},t)$ and $f_{II}(\vec{k},t)$ are the time-dependent momentum distribution functions in regions I and II, respectively, and F is the electric field applied.[44] The first term on the right-hand-side (RHS) of Eq. (2.1a) accounts for low-energy scattering mechanisms where,

$$f_o(\vec{k}) = \frac{1}{1+\exp(\frac{\hbar v_F(k-k_F)}{k_b T})} \qquad (2.2)$$

is the Fermi-Dirac equilibrium distribution function and $k_F > 0$ is the Fermi momentum so that only intraband processes restricted to the conduction band are considered. Interband processes will be the object of future work. Also, note that at room temperature, for Fermi levels at $E_F = k_B T$ above the Dirac point, the carrier concentrations is $n_c \approx 1.8$ x 10^{11} cm^{-2}. The parameter τ is the relaxation time[50] (for the sake of simplicity, it is assumed that τ is k-independent and it's value is varied compared to the OP scattering rate). $S(\vec{k}',\vec{k})$ is the OP transition rate from a state with momentum $\vec{k}'$ to the state with momentum $\vec{k}$, given by†[51,52]

$$S(\vec{k},\vec{k}') = \frac{\pi D_o{}^2 (N_q+1)\delta(E'-E+\hbar\omega_{OP})}{\sigma A \omega_{OP}} \qquad (2.3)$$

where D_o is an effective optical deformation potential accounting for intra and intervalley scattering. The parameter σ is the mass of the graphene sheet per unit area, and A is the area of the sheet.

The second term on the (RHS) of Eq. (2.1b) is the carrier depopulation by OP emission, while in Eq. (2.1a) it is the corresponding carrier repopulation at low energy. Here OP absorption processes are neglected since for temperature $T = 300$ K used throughout this analysis, $\hbar\omega_{OP} \gg k_B T$, for which the phonon occupation number N_q is negligible, so OP's only scatter electrons from region II to region I.

2.3 STEADY STATE REGIME

First, the solution for f_I and f_{II} under steady-state conditions is obtained by setting $\frac{\partial f_I(\vec{k},t)}{\partial t} = \frac{\partial f_{II}(\vec{k},t)}{\partial t} = 0$ in Eqs. (2.1a) and (2.1b). The procedure is to solve Eq. (2.1b) for f_{II}, and substitute it's value in Eq. (2.1a) to solve for f_I. Then one matches the two solutions at the boundary $k = k_c$.

---

† The transition rate should be multiplied by $(1 + \cos(\theta'))$, where θ' is the angle between $\vec{k}$ and $\vec{k}'$. The summation over $\cos(\theta')$ prohibits scattering to areas near $-k_x$ axis in region I. This, however does not introduce significant changes to the results.

The general solution of Eq. (2.1b) is then,

$$f_{II}(k_x, k_y) = f_I(k_x^0, k_y)\Upsilon(k_x, k_y) \tag{2.4}$$

where $f_I(k_x^0, k_y) = f_{II}(k_x^0, k_y)$ is the distribution function at the boundary and $k_x^0 = \sqrt{k_c^2 - k_y^2}$ is the k_x value at the boundary $k = k_c$. From here on, the transformation $k_x/k_c \to k_x, k_y/k_c \to k_y$, and $k_c \to 1$ will be used. In this framework, the function Υ is given by,

$$\Upsilon(k_x, k_y) = \exp\left\{-a\int_{k_x^0}^{k_x}\{\sqrt{z^2 + k_y^2} - 1\}dz\right\}$$

where the dimensionless parameter a is given by

$$a = \frac{D_o^2 k_c^2}{2\sigma\omega_{OP}eFv_F}.$$

Substituting Eq. (2.4) into Eq. (2.1a) leads to the following equation in region I:

$$\frac{\partial f_I}{\partial k_x} + a\gamma f_I = a\gamma f_o(k_x, k_y) + \frac{a(k+1)}{2\pi}\int_{-1}^{1} dy f_b(y)\frac{\Upsilon(k_{xc}, y)}{k_{xc}}, \tag{2.5}$$

where

$$k_{xc} = \sqrt{(k+1)^2 - y^2}$$

with

$$k = \sqrt{k_x^2 + k_y^2}$$

and the damping parameter γ is defined as

$$\gamma = \frac{\tau_o}{\tau},$$

where $\tau_o = \tau_{OP}(k = 1.5k_c)$ and

$$\frac{1}{\tau_{OP}(\vec{k})} = \sum_{\vec{k}'} S(\vec{k}, \vec{k}')$$

is the OP scattering rate. Using $\hbar\omega_{OP} = 0.2$ eV, $D_o = 14$ eV/$\mathring{A}$,[53] and $\sigma = 7.61$ x 10^{-7} kg/m^2, one finds $\tau_o \approx 0.32$ps. The preceding equation is a first-order partial differential equation with solution

$$f_I(k_x, k_y) = T_1(k_x, k_y) + \frac{a}{2\pi}\int_{-1}^{1} dy f_b(y)K(k_x, y, k_y), \tag{2.6}$$

10

where

$$T_1(k_x, k_y) = a\gamma e^{-a\gamma k_x} \int_{-1}^{1} dz f_o(z, k_y) e^{a\gamma z}$$

and

$$K(k_x, y, k_y) = e^{-a\gamma k_x} \int_{k_x^0}^{k_x} \frac{dz \Upsilon(k_{xc}(z), y)\{\sqrt{z^2 + k_y^2} + 1\}e^{a\gamma z}}{k_{xc}(z)}$$

with

$$k_{xc}(z) = \sqrt{(\sqrt{z^2 + k_y^2} + 1)^2 - y^2}.$$

Evaluating f_I at the boundary leads to an integral equation of the form

$$f_b(k_y) = T_1(k_x^0, k_y) + \frac{a}{2\pi} \int_{-1}^{1} f_b(y) K(k_x^0, y, k_y) dy. \tag{2.7}$$

With known functions $T_1(k_x^0, k_y)$ and $K(k_x^0, y, k_y)$, Eq. (2.7) is solved numerically, and the solution gives both, $f_I(\vec{k})$ and $f_{II}(\vec{k})$. Figure 2.2(a) is a contour plot of the steady-state distribution for different values

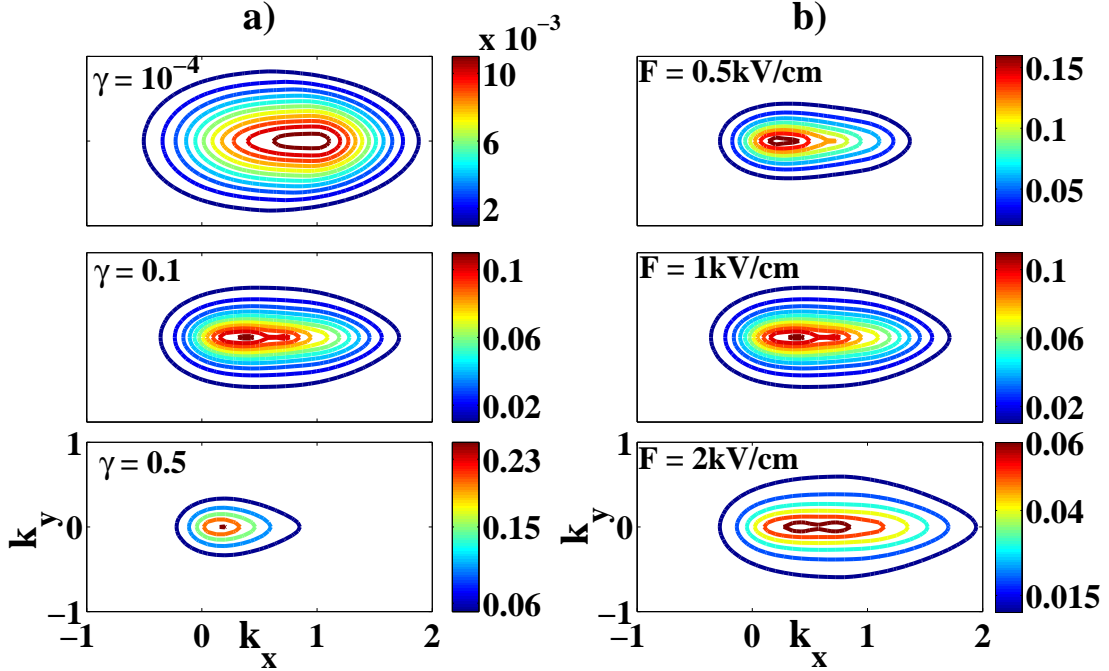**Figure 2.2:** (Color online) (a)Contour plot of the distribution functions for different damping parameters ($F = 1$ kV/cm) and (b)different applied fields ($\gamma = 0.1$).

of γ and $F = 1$ kV/cm. For negligible values of γ (top panel), the distribution is elongated toward the k_x axis, with its centroid located around $k_x = k_c$ ($k_x = 1$ on the figure). As the low-energy damping

11

increases($\gamma \rightarrow 0.5$), electrons scatter in the low-energy region (I) with a few of them reaching region II. The electron population concentrates around the distribution centroid that recedes towards $k_x = 0$ (bottom panel). Notice the color code is different for each panel. Figure 2.2(b) display similar contour plots for different electric fields and constant $\gamma = 0.1$. Here as the electric field is increased, the distribution is more and more elongated, and broader along the k_x axis, but an unexpected phenomenon occurs as the centroid of the distribution evolves into a double hump clearly seen in the bottom panel. This is a consequence of the high repopulation rate for high-energy electron close to $k_x = 2k_c$ ($k_x = 2$ on the figure).

Figure 2.3 is a plot of the current density in the high-field regime for different values of γ. As expected, the current decreases with damping and reaches it's saturation value at higher fields.

Steady State Current Density
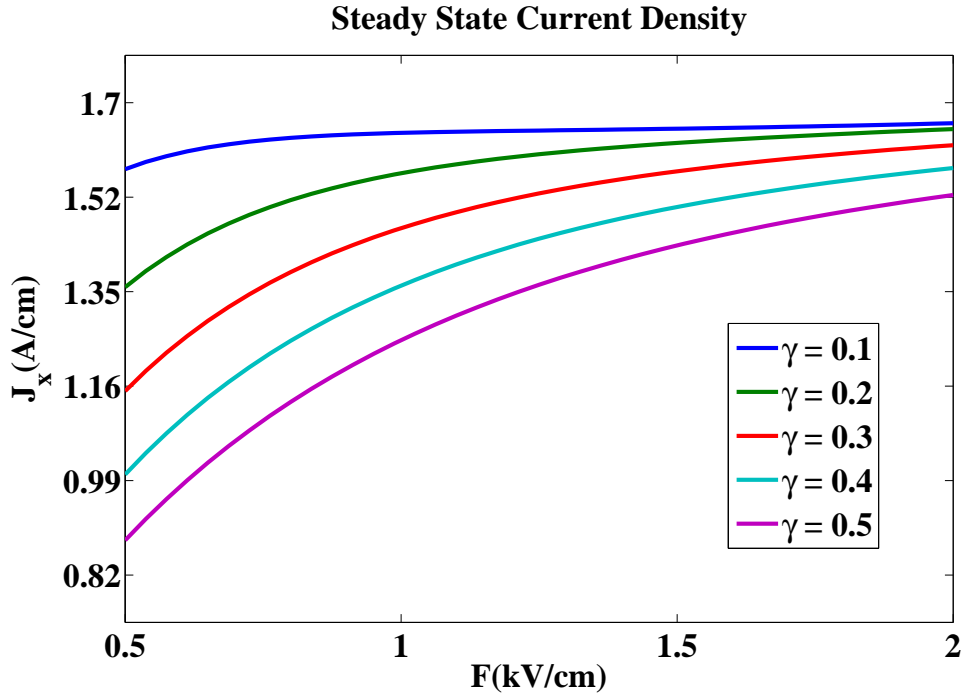
Figure 2.3: (Color online) Current density in the high field regime for different damping parameters. Here the carrier concentration in $n_c = 1.8 \times 10^{11}/\text{cm}^2$.

2.4 TRANSIENT REGIME

The substitution $u = t - \hbar k_x/eF$ is used to solve for the distribution function in the transient regime,

$$\frac{eF}{\hbar}\frac{\partial g_{II}(k_x, k_y; u)}{\partial k_x} = -\frac{g_{II}(k_x, k_y; u)}{\tau_{OP}(\vec{k})}, \tag{2.8}$$

where $g_{II}(k_x, k_y; u) = f_{II}(k_x, k_y, u + \hbar k_x/eF)$. The solution of Eq. (2.8) is then

$$g_{II}(k_x, k_y; u) = g_{II}(k_x^0, k_y; u) \exp\left\{-\frac{\hbar}{eF} \int_{k_x^0}^{k_x} \frac{dz}{\tau_{OP}(z, k_y)}\right\}. \tag{2.9}$$

Going back to the time variable, the general solution in region II is then

$$f_{II}(k_x, k_y, t) = f_{II}(k_x^0, k_y, t - \nu_o(k_x - k_x^0)) \exp\left\{-\frac{\hbar}{eF} \int_{k_x^0}^{k_x} \frac{dz}{\tau_{OP}(z, k_y)}\right\}, \tag{2.10}$$

where

$$\frac{1}{\nu_o} = \frac{eF}{\hbar}$$

is the "speed" with which the distribution moves towards the critical circle. Equation (2.10) describes a distribution that starts at the critical circle and moves in the direction of the electric field F with "speed" $1/\nu_o$, while decreasing exponentially as carriers emit OP's.

At $(t = 0)$, the distribution in region I is the Fermi-Dirac distribution,

$$f_I(k_x, k_y, t = 0) = f_o(k_x, k_y). \tag{2.11}$$

Right after the electric field is turned on, during the first trip towards the critical circle($0 \leq t < \nu_o k_c$), the inside distribution drifts towards the critical circle while undergoing low-energy scattering. During this trip, one assumes that all carriers are in region I, corresponding to $f_{II} \approx 0$. Using the coordinate transformation described earlier and the initial condition, the distribution in region I is given by

$$f_I^{(1)}(k_x, k_y, t) = f_o(k_x - t/\nu_o, k_y)e^{-\frac{t}{\tau}} + \frac{\nu_o}{\tau}e^{-\frac{\nu_o k_x}{\tau}} \int_{k_x - t/\nu_o}^{k_x} dz e^{\frac{\nu_o z}{\tau}} f_o(z, k_y). \tag{2.12}$$

One then uses the boundary condition $f_I(k_x^0, k_y, t) = f_{II}(k_x^0, k_y, t)$[54] and Eq. (2.10) to obtain the distribution in region II:

$$f_{II}^{(1)}(k_x, k_y, t) = f_I^{(1)}(k_x^0, k_y, t - \nu_o(k_x - k_x^0)) \exp\left\{-\frac{\hbar}{eF} \int_{k_x^0}^{k_x} \frac{dz}{\tau_{OP}(z, k_y)}\right\}. \tag{2.13}$$

The preceding equation describes carriers in region II that interact with OP and scatter into region I. For $t \geq \nu_o k_c$, the solution $f_{II}^{(1)}(\vec{k}, t)$ is substituted into the integral of the right hand side of Eq. (2.1a) to start

13

the same procedure, with the same variable substitution $u = t - \nu_o k_x$, for later times to get

$$f_I^{(2)}(k_x, k_y, t) = \frac{\nu_o}{\tau} e^{-\frac{\nu_o k_x}{\tau}} \int_{-k_x^0}^{k_x} f_o(z, k_y) e^{\frac{\nu_o z}{\tau}} dz$$

$$+ \nu_o e^{-\frac{\nu_o k_x}{\tau}} \int_{-k_x^0}^{k_x} \sum_{\vec{k}'} S(\vec{k}', z, k_y) f_{II}^{(1)}(\vec{k}', t - \nu_o(k_x - z)) e^{\frac{\nu_o z}{\tau}} dz \qquad (2.14)$$

for the second distribution in region I. This distribution is accelerated towards the critical circle and the process repeats itself.

As the electron population moves back and forth between regions I and II, it undergoes each time more dephasing and broadening due to the finite duration of the OP emission process. The distribution function in each region at any time t corresponding to the nth trip toward the critical circle, that is, for $n = integer[eFt/\hbar k_c] + 1$, can be written as a superposition of distributions $f_I^{(i)}(k_x, k_y, t)$ and $f_{II}^{(i)}(k_x, k_y, t)$ of individual i^{th} "trip", that is,

$$f_I(k_x, k_y, t) = \sum_{i=1}^{n} f_I^{(i)}(k_x, k_y, t) \qquad (2.15a)$$

and

$$f_{II}(k_x, k_y, t) = \sum_{i=1}^{n} f_{II}^{(i)}(k_x, k_y, t). \qquad (2.15b)$$

The whole distribution is then normalized to the total carrier concentration n_c.

2.5 RESULTS

The dimensionless time parameter $\tilde{t}$ will be used to describe the results:

$$\tilde{t} = \frac{t}{t^*},$$

where

$$t^* = \nu_o k_c$$

is the approximate time taken for the distribution to complete one "trip". The results are presented in terms of the normalized coordinates, $k_x/k_c \to k_x, k_y/k_c \to k_y$, and $k_c \to 1$.

Figure 2.4(a) shows the time evolution of the distribution function (DF) for $F = 1$ kV/cm ($t^* \approx 2$ ps), in the absence of low energy scattering ($\gamma = 0$). At $\tilde{t} = 0(t = 0)$, the initial distribution is the tail of the Fermi distribution in the conduction band [Eq. (2.2)], which is Maxwellian-like, and drifts along the k_x direction (opposite to the F field) to reach the OP energy at $\tilde{t} = 1$ (second panel). At that time, a "hump"
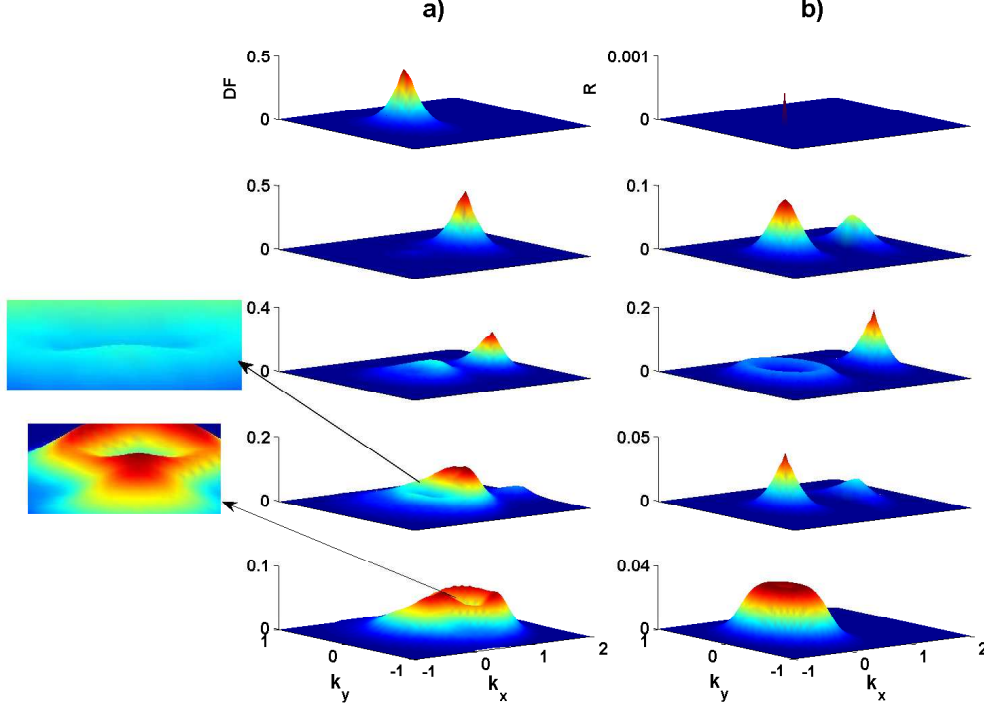
14

Figure 2.4: (Color online) a) 3D plots of the distribution function at different times ($\tilde{t} = 0$, 1, 1.5, 2, and 2.5) for $F = 1$ kV/cm and vanishing low- energy scattering ($\gamma = 0$). b) Corresponding depopulation and repopulation rates for the same times as in (a).

appears around $k = 0$ (not yet visible on the DF graph) as the front electrons reach region II, where they emit OP's and scatter back inside region I, as seen in the second panel of Fig. 2.4(b). As time progresses $\tilde{t} = 1.5$, the "hump" develops into a dimple, while the remaining high-energy electrons from the first trip continue their drift in region II, where they experience strong OP depopulation. As seen in the third panel of Fig. 2.4(b), the corresponding repopulation rate at low energy exhibits a craterlike shape, which is due to the randomizing nature of the deformation potential OP scattering. Indeed, as schematically shown in Fig. 2.1(b), after OP emission by high-energy electrons, all $|\vec{k} - \vec{k}_c|$ values become equiprobable, which forms a drifting circle of high repopulation rate, with increasing k radius as first trip electrons penetrate deeper in region II. This craterlike feature of the repopulation rate is the primary cause of the dimple in the low-energy distribution function, which are areas in k space where electrons have low probability to scatter. As time progresses, the DF "dimple" evolves into a crater-like shape, [Fig. 2.4(a), fourth and fifth panel], and the successive depopulation-repopulation OP processes overlapping at low energy with different amplitudes form also smooth terraces in the low-energy tail of the distribution as it approaches steady state [Fig. 2.4(a) , fourth panel]. These morphological effects in electron distribution are unique to graphene as a result its linear band structure and the interplay of the quasiballistic acceleration and relaxation by
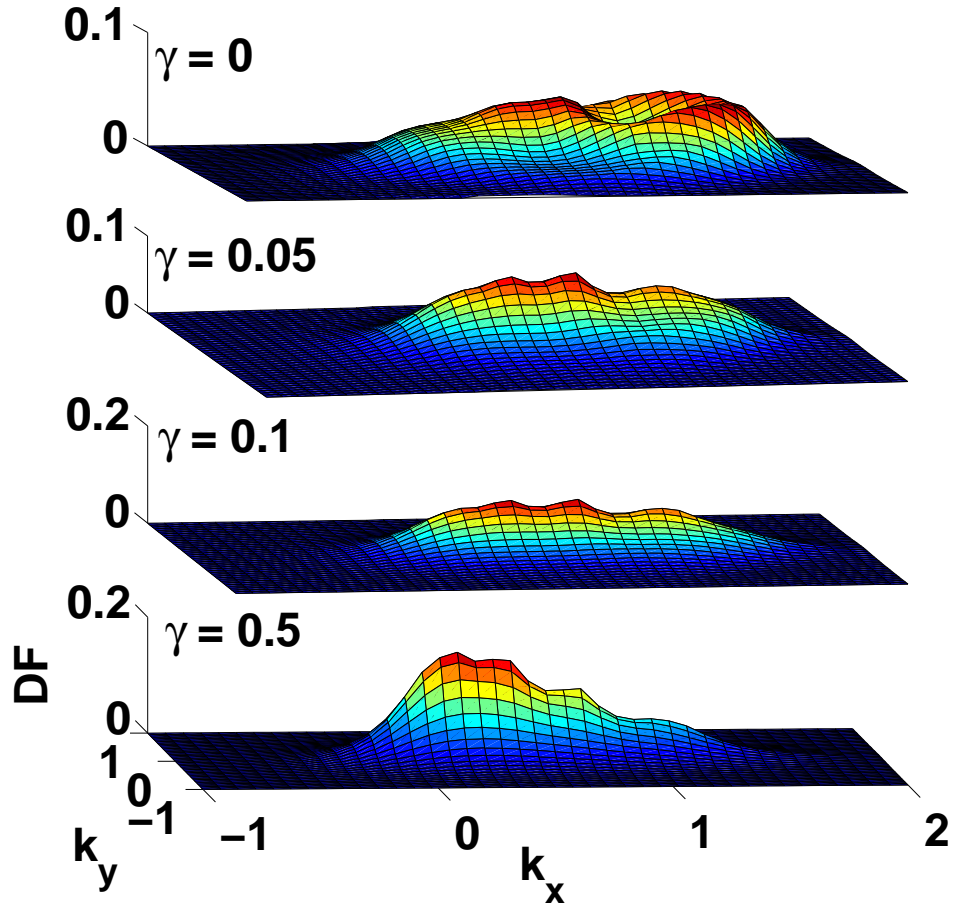
Figure 2.5: (Color online) 3D plots of the distribution functions at $\tilde{t} = 2.5$ for $\gamma = 0$, 0.05, 0.1, and 0.5. The applied field is $F = 1$ kV/cm.

high-energy monochromatic OP's.
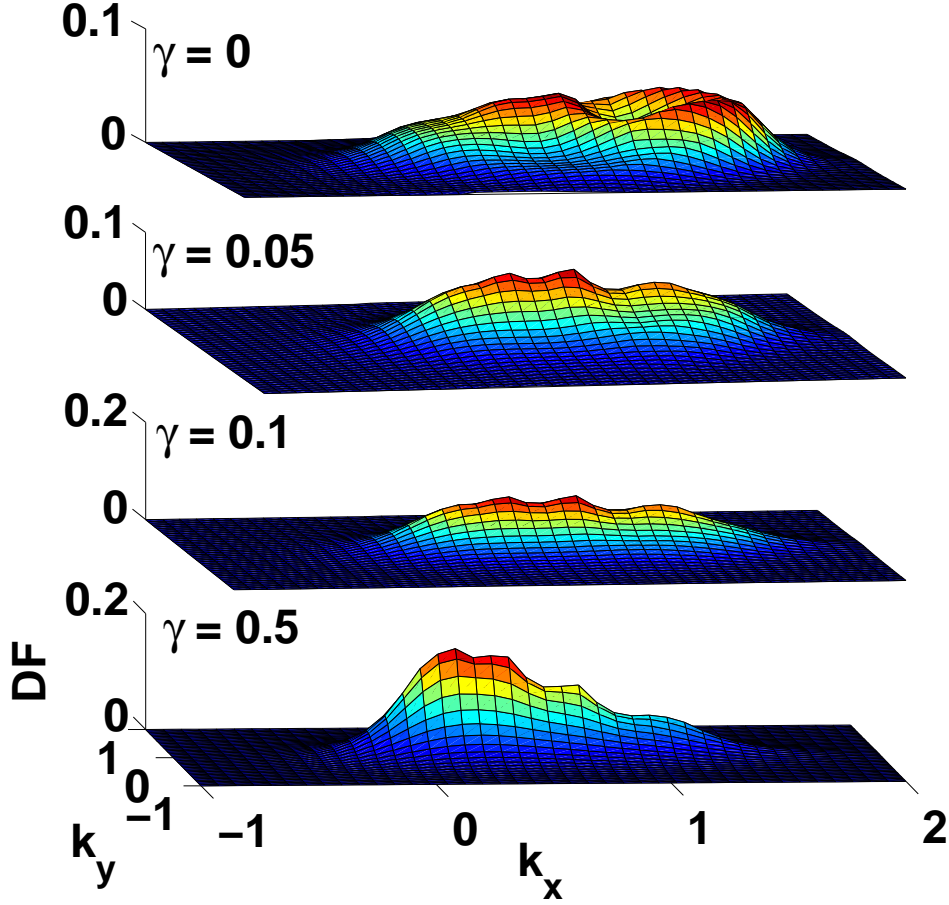
Figure 2.6: (Color online) 3D plots of the distribution functions at $\tilde{t} = 2.5$ for $\gamma = 0$, 0.05, 0.1, and 0.5. The applied field is $F = 1$ kV/cm.

Figure 2.5 shows snapshots of the distribution function at $\tilde{t} = 2.5$ for varying low energy relaxation-time, expressed in terms of $\gamma = \tau_0/\tau$. From the figure, one can see that the crater in the DF that occurs for $\gamma = 0$ progressively disappears as γ increases. Indeed low- energy scattering in region I redistributes charge-carrier momenta around $\vec{k} = 0$, especially in the crater center. For these reasons, the amplitude of the distribution in region I increases around $\vec{k} = 0$. Also, the distribution amplitude decreases in region II $(k > k_c)$ as carriers spend more time in region I $(k \leq k_c)$. Similarly, the distribution recovers a streaming profile along the k_x direction as conventional semiconductors.[41,54] Nevertheless, even for strong damping $(\gamma = 0.5)$, the distribution is characterized by a jagged profile, which contains the front and back ridges of the crater remnant still caused by the cumulative effects of the OP scattering for backward and forward carrier relaxation.

17

Figure 2.7: (Color online) a) Current density as a function of time for different values of the low-energy scattering parameters $\ga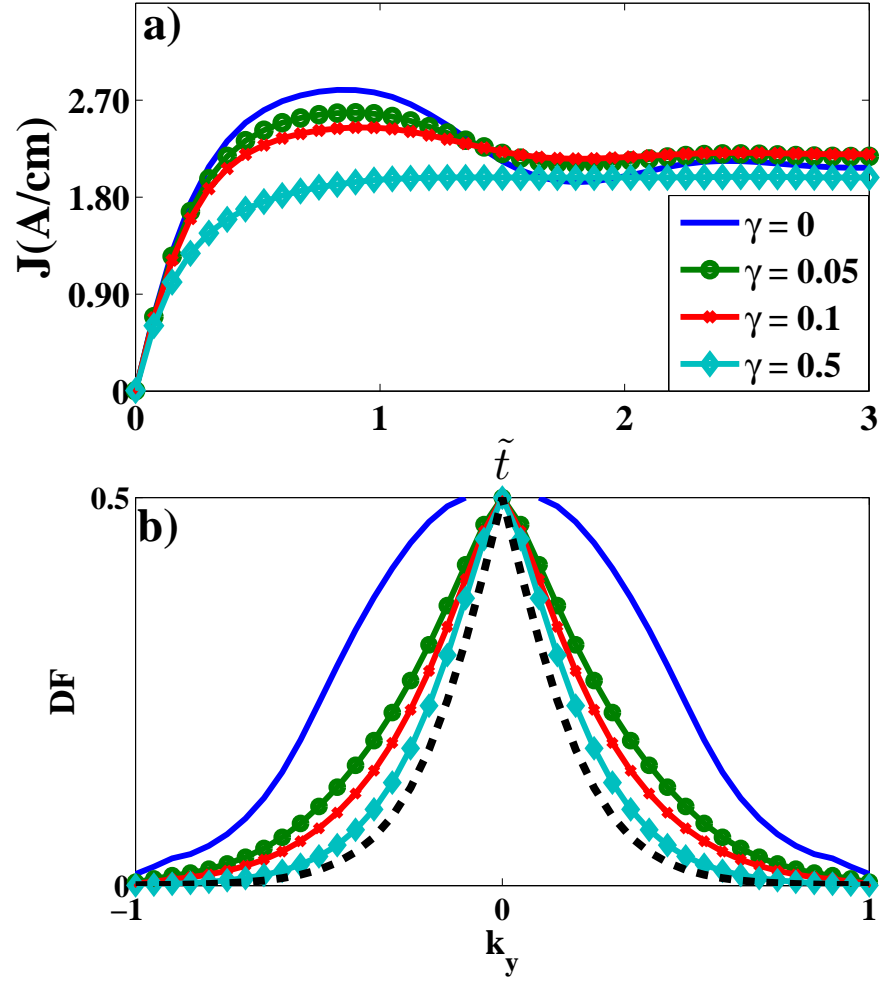mma$. The applied field is $F = 1$ kV/cm. b) Cross sections of the distribution at $\tilde{t} = 3$ and $k_x = 0.5k_c$ for the corresponding values of γ. Dash lines: initial distribution function at $k_x = 0$.

The current density on the plane is given by,

$$J_x(t) = -4ev_F \sum_{\vec{k}} f(\vec{k}, t) \cos(\phi), \tag{2.16}$$

where ϕ is the angle between $\vec{k}$ and the k_x axis. Figure 2.6(a) shows the current density as a function of time ($\tilde{t}$) for $F = 1$ kV/cm and different low-energy scattering rates. For weak scattering, the current density overshoots its steady-state value through damped oscillations, as a result of the back-and-forth motion of the distribution function (Fig. 2.1). The weaker the scattering, the higher the current overshoot. For strong low-energy scattering, the current converges monotonically toward its steady-state value without oscillations.[41] Notice that the stronger the scattering, the lower the steady-state current value. Figure 2.6(b) shows the corresponding DF cross-sections at $k_x = 0.5$ and $\tilde{t} = 3$ relative to the initial distribution at $k_x = 0$. As low-energy scattering increases, the DF becomes narrower, taking a "streaming" profile in the electric-field direction. This is due to the fact that as the low-energy scattering increases, fewer electrons reach the high energy ($E \geq \hbar\omega_{OP}$) region II, reducing the number of electrons scattered back to the low-energy region I, which narrows the distribution.

Figure 2.7 shows the current density as a function of time for three different field values, with $\gamma = 0.05$ in each case. One observes that the oscillation period $\tau_{gr} = \hbar\omega_{OP}/eFv_F$ scales with the inverse of the electric field F. Also quite expectedly, the overshoot value increases with electric fields, but the damping is also enhanced with electric fields, which is due to the fact that the electron distribution penetrates the high-energy ($E \geq \hbar\omega_{OP}$) region(II) farther than $\hbar\omega_{OP}$, stretching the carrier relaxation by OP emission, which in turn broadens the DF in region I along the field, thereby reaching steady state quicker. Figure 2.7(b) shows the DF cross sections at $k_x = 0.5$ and $\tilde{t} = 3$ for the different fields, relative to the initial distribution at $k_x = 0$. As the field is increased, the distribution function broadens, because more electrons reach the high-energy ($E \geq \hbar\omega_{OP}$) region II, and scatter back into region I broadening the distribution in the process.

Note that, for $\hbar\omega_{OP} = 0.2$ eV and $F = 1$ kV/cm, the period of oscillations $\tau_{gr} = \hbar\omega_{OP}/eFv_F = 2$ ps corresponds to oscillation frequencies just below the terahertz range. Also, for the low damping case $\gamma = 0$ in Fig. 2.6(a), the maximum current density corresponds to carrier velocity $v \approx 0.95v_F$.

The average energy density of carriers in the conduction band is given by

$$E(t) = 4\hbar v_F \sum_{\vec{k}} k f(\vec{k}, t), \tag{2.17}$$

19
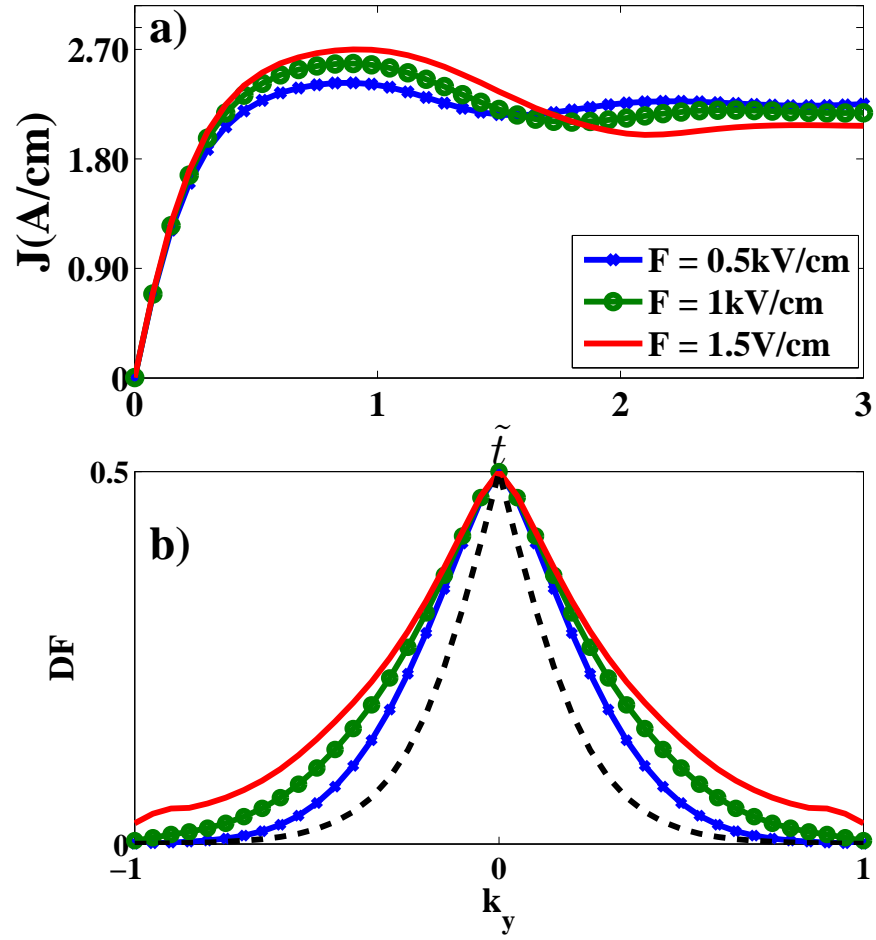
Figure 2.8: (Color online) a) Current density as a function of time for different fields and $\gamma = 0.1$. b) Cross section of the distribution function at $\tilde{t} = 3$ and $k_x = 0.5k_c$ for the corresponding values of F. Dash lines: initial distribution function at $k_x = 0$.
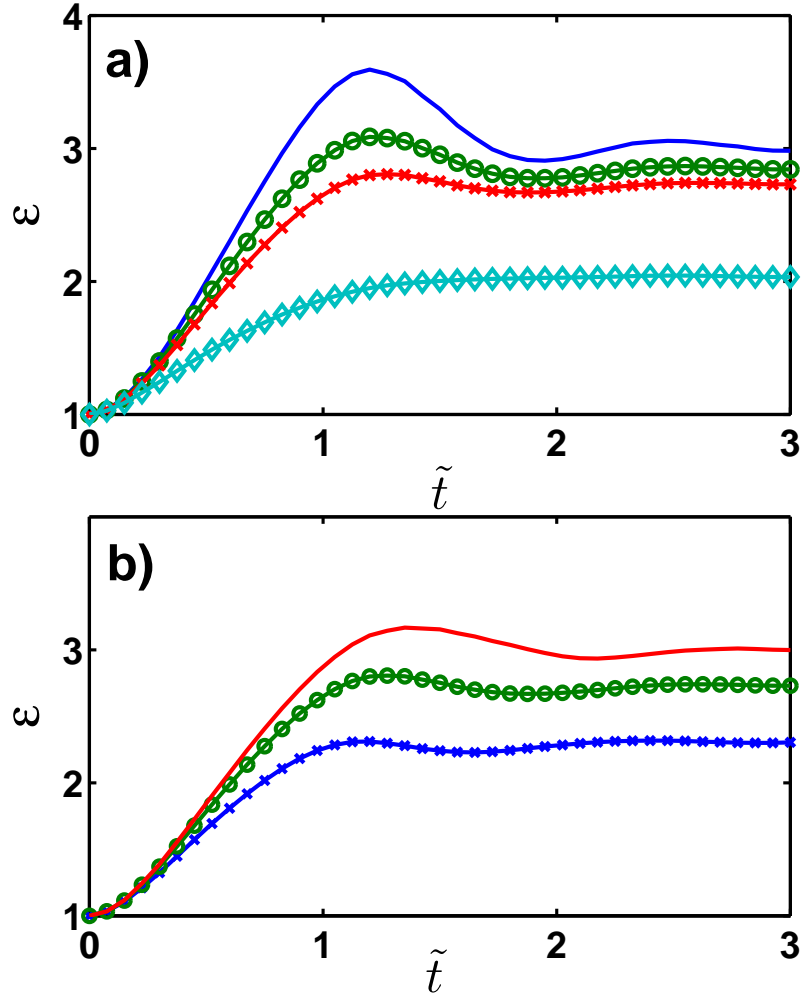
Figure 2.9: (Color online) Normalized value of the carrier energy as a function of time for different values of the low-energy scattering parameters γ. Solid ($\gamma = 0$), circles ($\gamma = 0.05$), crosses ($\gamma = 0.1$), and diamonds ($\gamma = 0.5$). The applied field is $F = 1$ kV/cm. b) Same as (a) but for different applied fields and $\gamma = 0.1$: Solid ($F = 1.5$ kV/cm), circles ($F = 1$ kV/cm), crosses ($F = 0.5$ kV/cm).

where $f(\vec{k}, t)$ is the overall normalized distribution function, and the summation is taken over all $\vec{k}$ in regions I and II. At $\tilde{t} = 0$, the average energy per charge carrier is found to be $E(0) \approx 2.2 k_B T$. This value is roughly twice larger than $k_B T$ expected for two-dimensional systems, and is the direct consequence of the linear energy dispersion in graphene, by contrast to the parabolic dispersion in normal 2D systems. Figure 2.8(a) displays the ratio $\epsilon = E(\tilde{t})/E(0)$ for $F = 1$ kV/cm and different low-energy scattering rate (γ). As expected, the energy converges to higher values as low-energy scattering is reduced. In addition, the convergence toward steady state occurs through damped oscillations, even for $\gamma = 0$ as a consequence of the back-and-forth motion of the DF between the OP energy and the carrier zero-point energy. Quite clearly the oscillation period is given by t^* for all γ. It is also seen that the oscillations persist even with significant low-energy scattering. Figure 2.8(b) displays the normalized energy ϵ as a function of time for different fields and $\gamma = 0.1$. As expected, carrier energies reach higher values as the field is increased, and the oscillation period decreases (larger $\tilde{t}$-period).

2.6   DISCUSSIONS

A transient analysis of the onset of current oscillations at the electric field turn-on caused by the back-and-forth motion of carrier distribution function between the zero-point energy and OP's in the presence of varying damping mechanisms has been provided. In this context, the anomalous shape of the carrier distribution is due to an interplay between ballistic acceleration and deformation potential OP emission in the transient regime. If OP-limited current oscillations have been predicted in GaAs,[41] and indirectly observed in slightly n-doped InSb,[42] their manifestation in graphene is different in several respects: First, owing to the linear carrier energy-momentum dispersion, the oscillation periodicity is given by $\tau_{gr} = \hbar \omega_{OP}^{gr}/eF v_F$ in graphene, while in a GaAs parabolic conduction band it is expressed as $\tau_{GaAs} = \sqrt{2m^* \hbar \omega_{OP}^{GaAs}}/eF$, which nevertheless yields similar values, since the small effective mass, and the OP phonon frequency in GaAs compensate for the large v_F.[41,44] Second, in III-V semiconductors, the OP polar nature focuses the low-energy repopulation along the k_x axis, which provides a "streaming" profile to the carrier distribution instead of a crater-like shape in this case. Finally, in compound semiconductors, the oscillation onset is restricted by two conflicting conditions: On the one hand, the low value of the OP energy ($\hbar \omega_{OP} : 0.04$ eV) is comparable to the thermal broadening of the carrier distribution at room temperature so that the back-and-forth motion of the distribution between the optic phonon and the zero-point energy is immediately damped.[41,43,44] On the other hand, at low temperature, ionized impurity scattering becomes dominant and produces strong damping which can only be reduced by lowering the dopant density, thereby lowering the

carrier density, and weakening the oscillation amplitude. In this respect, the high conductance of graphene, and the high optic phonon energy provide the conditions for room-temperature observation.

Low-energy scattering should however still be minimized. Usually, for experimental studies and device applications, graphene layers rest on a dielectric substrate, or are confined between two dielectric slabs.[55,56] In this case the presence of high K dielectrics sandwiching the strictly 2D graphene layer may be used to screen charged impurity that may reduce low-energy elastic scattering.[57] However, dielectrics also contain interface and remote static charges that may offset dielectric screening.[58] Moreover, the interaction between the 2D carriers in graphene and low-energy Remote Interface Phonon (RIP) arising from the proximity of the substrate[59,60] introduces new scattering sources.[48,61] Therefore in general, suspended graphene-layers avoiding the RIP influence may be preferable.[49,62]

In this context to be observable at room temperature, the velocity oscillations should also take place within a parameter window. On the one hand the process requires $eV > \hbar\omega_{OP}$ where V is the external bias, to reach the OP energy, and on the other hand, the field should be large enough for carriers to escape low-energy scattering, but $\hbar\omega_{OP}/eFv_F\tau_{OP} \gg 1$ where $1/\tau_{OP}$ is the OP scattering rate, so that charge carriers do not penetrate the high-energy region $E \geq \hbar\omega_{OP}$, scatter immediately after they reach the OP energy, which maintains the coherence of the distribution function. These requirements impose a lower and upper bound on the electric field, i.e. 0.5 kV/cm $< F \ll$ 5 kV/cm (in graphene), and a lower bound on the sample length $L > v_F\tau_{OP}$ ($> 1\mu$m for $\tau_{OP} < 1$ ps), but L should be smaller than a few values of $\lambda = \hbar\omega_{OP}/eF$, so as to prevent oscillation damping.

One important issue for the validity of this analysis is the effect of leakage current due to electrons in the valence band crossing to the conduction of carriers through the Dirac point. Indeed it has been shown that there is still a minimum conductance ($G \sim 4e^2/h$) between the two bands despite the singular nature of the Dirac point.[63] This value was later measured to be $G \sim e^2/h$.[24] However, this effect becomes important only when the graphene layer width $w \geq 23\mu m$, for which the band gap $E_g \leq 0.18$ meV are vanishing. Moreover, thermal effects such as acoustic phonon absorption by carriers in the valence band, are forbidden by conservation of both, energy and momentum. As for OP absorption it has been shown earlier (see Sec. II) their occupation number is also negligible over the time scale considered in this analysis.

Chapter 3

SOFT PARAMETRIC RESONANCE FOR HOT CARRIERS IN GRAPHENE*

3.1 INTRODUCTION

In high electric fields F, it is well known that carriers in graphene can accelerate ballistically before being scattered by high-energy optical phonons (OP's) ($\hbar\omega_{OP} \sim 0.2$ eV) causing carrier velocity saturation.[40,39] This produces a back-and-forth motion of carriers in k space between monochromatic OP energy and the Dirac point with a time period $\tau_F = \hbar\omega_{OP}/eFv_F$,[41,64] which results in a carrier velocity overshoot[65] and even damped oscillations during the transient to steady state, when the field is suddenly turned on.[41,64] While these oscillations were predicted to occur in GaAs at low temperature so that $\hbar\omega_{OP} \gg k_B T [\hbar\omega_{OP}(\text{GaAs}) = 36$ meV] they were limited to low fields ($F \sim 50\text{-}100$ V/cm, $\tau_F \sim 30$ ps)[41] to prevent intervalley scattering, whereas strong Coulomb scattering arising from the charged dopants would offset the effect. In graphene, the absence of an energy gap guarantees carriers without requiring dopants, while the large OP energy and weak acoustical-phonon (AP) scattering[66] allows its manifestation at room temperature with ramifications in THz technology, since the oscillation frequency $\omega_F = 2\pi/\tau_F \propto F \sim 1$ THz ($F = 2$ kV/cm) is tunable with the electric field. If a periodic (ac) field is superposed onto the dc field, the frequency of the back-and-forth carrier motion is modulated by the ac frequency, as a parametric oscillator. As a result, the amplitude of the carrier velocity or current oscillations is expected to be resonantly enhanced when the ac frequency ω matches a particular value η of the natural frequency ω_F, i.e., $\omega = \eta\omega_F$.[67] However, there are distinct differences between the usual parametric resonance (PR) and this type of hot-carrier resonance: First, the natural oscillations are strongly damped as a result of the probabilistic nature of the carrier-OP interaction that relaxes carrier energy at different times and momenta once they reach, and even overshoot the OP energy. Second, the system is strongly dissipative as the OP relaxation is responsible for bringing back the carriers to the low-energy Dirac point. Consequently, the resonance is anticipated to be "soft" i.e. with a broad peak in the oscillation amplitude vs ω, and to manifest for different η values than normal PR.

Because of these distinctive features, it is shown in this chapter that the anomalous nature of this type
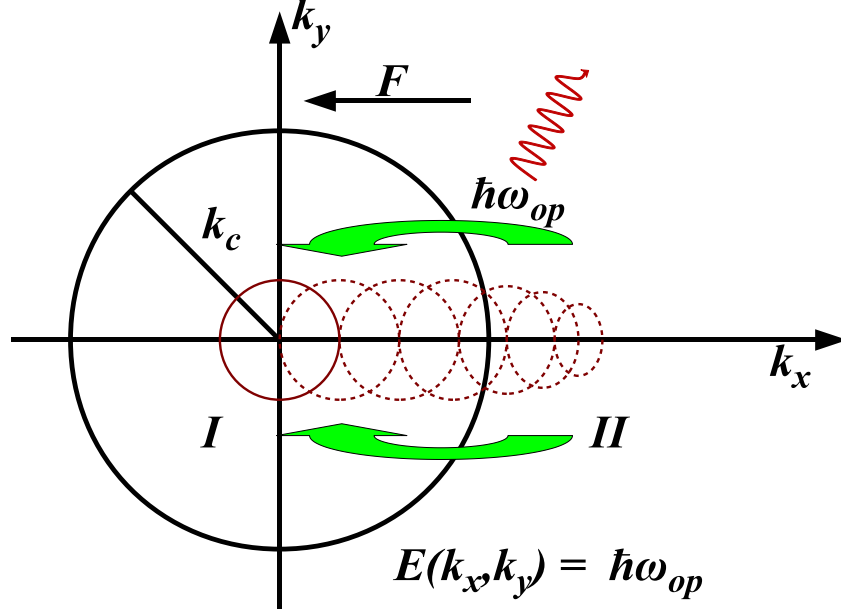

Figure 3.1: (Color online) Quasiballistic carrier acceleration followed by OP scattering in the 2D k space of graphene. The circle corresponds to the electronic energy $\hbar\omega_{OP}$.

of resonance that manifests for $\eta \sim 1/2$ instead of $\eta \sim 2$ in normal PR.[67] We also find that the dephasing between the current and ac field exhibits a minimum as a function of the ac field frequency for weak damping by AP or other low-energy scattering, and softens to become monotonic at high damping for all ac field strengths.

3.2 OPTIC-PHONON SCATTERING AND HOT CARRIER-MODEL

Consider a system of electrons in the conduction band of graphene under the influence of a spatially homogeneous and time-dependent electric field $F(t)$. The electric field takes the form $F(t) = F_o + F_1 \cos(\omega t)$ and is applied along the positive k_x direction, where F_o is a permanent constant field, F_1 is a constant such that $0 < F_1/F_o < 1$, and ω is the frequency of the applied field. The momentum space is divided into the low (I) and high (II) energy regions bounded by the critical momentum k_c that corresponds to electron energy $\hbar v_F k_c = \hbar\omega_{OP}$ (Fig. 3.1). In the low-energy region I, charge carriers are ballistically accelerated towards the critical circle k_c while interacting with low-energy scattering agents (e.g., AP's or impurities). In the high-energy region II, the carriers lose all their energy by OP emission and are scattered back into the low-energy region. For this process to occur, the electric-field maximum is low enough such that electrons

move back and forth between regions I and II only, with negligible probability to reach $E \geq 2\hbar\omega_{OP}$.

Because of the probabilistic nature of carrier transport, a large-signal Boltzmann transport equation (BTE) that accounts for low-energy scattering (damping), e.g., by impurities and AP will be solved.[47,64] The BTE in the two regions can be written as[64]

$$\frac{\partial f_I(\vec{k},t)}{\partial t} + \frac{eF(t)}{\hbar}\frac{\partial f_I(\vec{k},t)}{\partial k_x} = -\frac{f_I(\vec{k},t) - f_o(\vec{k})}{\tau_{LE}} + \sum_{\vec{k}'} S_{OP}(\vec{k}',\vec{k})f_{II}(\vec{k}',t), \tag{3.1a}$$

$$\frac{\partial f_{II}(\vec{k},t)}{\partial t} + \frac{eF(t)}{\hbar}\frac{\partial f_{II}(\vec{k},t)}{\partial k_x} = -f_{II}(\vec{k},t)\sum_{\vec{k}'} S_{OP}(\vec{k},\vec{k}'), \tag{3.1b}$$

where $f_I(\vec{k},t)$ and $f_{II}(\vec{k},t)$ are the time-dependent momentum distribution functions (DF) in the low- and high-energy regions, respectively, and e is the electronic charge. Equation (3.1a) describes electron transport at low energy, where the left-hand side (LHS) accounts for the transient drift, while the first term on the right-hand side (RHS) accounts for low energy scattering, i.e, AP and impurities scattering. The second term on the RHS of Eq. (3.1a) accounts for low energy carrier repopulation caused OP emission. Equation (3.1b) describes electron transport at high energy ($E \geq \hbar\omega_{OP}$), where the LHS and the RHS account for transient drift, and electron depopulation due to OP emission, respectively.[64] In Eq. (3.1a), the function $f_o(\vec{k})$ is the Fermi-Dirac DF ($k_F > 0$), $S_{OP}(\vec{k},\vec{k}')$ is the OP transition rate between the states $\vec{k}$ and $\vec{k}'$, and τ_{LE} is the relaxation time.[64] In this analysis, the temperature of the graphene sample is assumed to be $T = 300$ K, so $n_q \ll 1$ and phonon absorption can be neglected. However, it is observed that the model is also valid at lower T, as the DF profile larger than the thermal broadening is essentially determined by high-field carrier dynamics, as long as the Coulomb scattering (dopant concentration) can be kept weak, as shown in Ref. 68 and later on in this analysis. Note that at this temperature, and if we choose $E_F = k_B T$ above the Dirac point in $f_o(\vec{k})$, the carrier concentration is $n_c \approx 1.8$ x 10^{11} cm^{-2}, which is low enough to neglect intercarrier scattering on the DF. Moreover, the hole concentration is even smaller to significantly affect the carrier dynamics in the conduction band so that interband transition can be neglected.[69]

3.2.1 Self-Consistent Solution of Boltzmann Transport Equation

The procedure is to solve Eq. (3.1b) for $f_{II}(\vec{k},t)$ and substitute the solution in Eq. (3.1a) to solve for $f_I(\vec{k},t)$.[44,64] The DFs in the two regions are then matched on the boundary $k = k_c$.

By using the substitution $\kappa = k_x + \beta(t)$, where,

$$\beta(t) = -\frac{e}{\hbar} \int_0^t F(s)ds, \tag{3.2}$$

the LHS of Eq. (3.1) transforms into $eF(\beta^{-1}(\kappa - k_x))\partial g_{I,II}/\hbar \partial k_x$, where $g_{I,II}(k_x, k_y; \kappa) = f_{I,II}(k_x, k_y, \beta^{-1}(\kappa - k_x))$, and β^{-1} is the inverse function of β so that $\beta^{-1}\beta(t) = t$. Consequently, the general solution of Eq. (3.1b) takes the form

$$f_{II}(k_x, k_y, t) = f_b(k_y, \beta^{-1}(\beta(t) + k_x - k_x^0))M(k_x, k_y, t), \tag{3.3}$$

where $f_b(k_y, t) = f_{II}(k_x^0, k_y, t)$ is the time dependent DF evaluated at the boundary $k = k_c$, and $k_x^0 = \sqrt{(k_c)^2 - (k_y)^2}$. The $M(k_x, k_y, t)$ factor given by

$$M(k_x, k_y, t) = \exp\left\{ -\frac{\hbar}{e} \int_{k_x^0}^{k_x} \frac{dp\, \tau_{OP}^{-1}(p, k_y)}{F[\beta^{-1}(\beta(t) + k_x - p)]} \right\}$$

is the decay function caused by OP emission of hot carriers, and $1/\tau_{OP}(\vec{k}) = \sum_{\vec{k}'} S_{OP}(\vec{k}, \vec{k}')$. Equation (3.3) is then substituted into Eq. (3.1a) to solve for $f_I(\vec{k}, t)$. The matching conditions $f_b(k_y, t) = f_I(k_x^0, k_y, t) = f_{II}(k_x^0, k_y, t)$ of the two solutions f_I and f_{II} at the boundary leads to an integral equation of the form

$$f_b(k_y, t) = f_b^1(k_y, t) + \frac{\hbar}{(2\pi)^2 e} \int_{-k_x^0}^{k_x^0} dp \int d\vec{k}'\, S_{OP}(\vec{k}', \vec{k})\Big|_{k_x=p} f_{II}(\vec{k}', t') \exp\{\frac{t'-t}{\tau_{LE}}\}/F(t'), \tag{3.4}$$

where the function $f_b^1(k_y, t)$ is the solution $f_I(k_x^0, k_y, t)$ in the absence of OP scattering, and t' is a retarded time such that $\beta(t') = \beta(t) + k_x^0 - p$ (see Supplementary Material in Ref. 70). The second term on the RHS of Equation (3.4) accounts for the contribution of OP emission to the DF at the boundary, and the summation is taken over states $\vec{k}'$ in the high-energy region. Eq. (3.4) is solved by iteration, and the solution for $f_b(k_y, t)$ is expressed as a series,

$$f_b(k_y, t) = f_b^1(k_y, t) + f_b^2(k_y, t) + f_b^3(k_y, t) + \dots \tag{3.5}$$

which converges since the function $M(k_x, k_y, t)$ is a decreasing exponential and $f_b^n \propto (1/2\pi)^{n-1}$. The solution for $f_b(k_y, t)$ used throughout this analysis is obtained by neglecting terms of $O((1/2\pi)^3)$ and higher in the series (3.5). Once $f_b(k_y, t)$ is known, the DFs in both regions are readily obtained.

The two-dimensional (2D) current density on the plane is given by

$$J_x(t) = -4ev_F \sum_{\vec{k}} f(\vec{k}, t) \cos(\phi), \tag{3.6}$$

where ϕ is the angle between $\vec{k}$ and the k_x axis, and $f(\vec{k}, t)$ is the DF in the two regions.

3.3 RESULTS

In this analysis, the value $F_o = 1$ kV/cm is used and the applied frequency is expressed in units of ω/ω_F. A dimensionless damping parameter γ to gauge the strength of low-energy scattering is defined as $\gamma = \tau_{OP}(k = 1.5k_c)/\tau_{LE}$.[64] Also, τ_{OP} for $k = 1.5k_c$ is chosen as the intermediate value between k_c and $2k_c$ as $1/\tau_{OP}(k_c) = 0$.
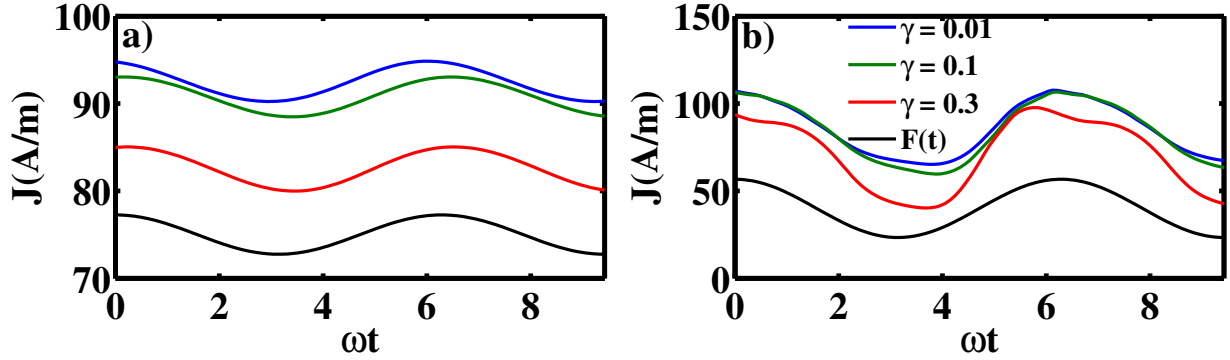

Figure 3.2: (Color online) Current density for three different values of the damping γ at resonance($\omega \approx 0.56\omega_F$). (a) $F_1/F_o = 0.1$; (b) $F_1/F_o = 0.8$.

Figure 3.2 shows the current density versus time for different values of γ and two field strengths at resonance, i.e., when $\omega \approx 0.56\omega_F$ (see Fig. 3.3). It is seen that the amplitudes of current density oscillations increase as the applied field F_1 increases compared to F_o as a larger population of electrons escapes low-energy scattering to reach the OP energy. At the same time, electrons also reach lower velocities during the negative cycles of F_1. For this reason, the current density swing increases with F_1/F_o. One also notices distortions in the current density oscillations at large fields [Fig. 3.2(b)] as the electron population competes between the natural oscillations at ω_F and the oscillations imposed by the F_1 field. As expected, it is also seen that the current density amplitude decreases with increasing γ as a result of increased electron scattering in the low-energy region, thereby lowering the carrier velocity.

Figure 3.3 shows plots of current density amplitude versus frequency for different values of γ and F_1/F_o. In the figure, the amplitude is defined as the difference between the maximum and minimum values of the current density. As seen from the plots, parametric resonance is achieved when $\omega/\omega_F \approx 0.56$. This
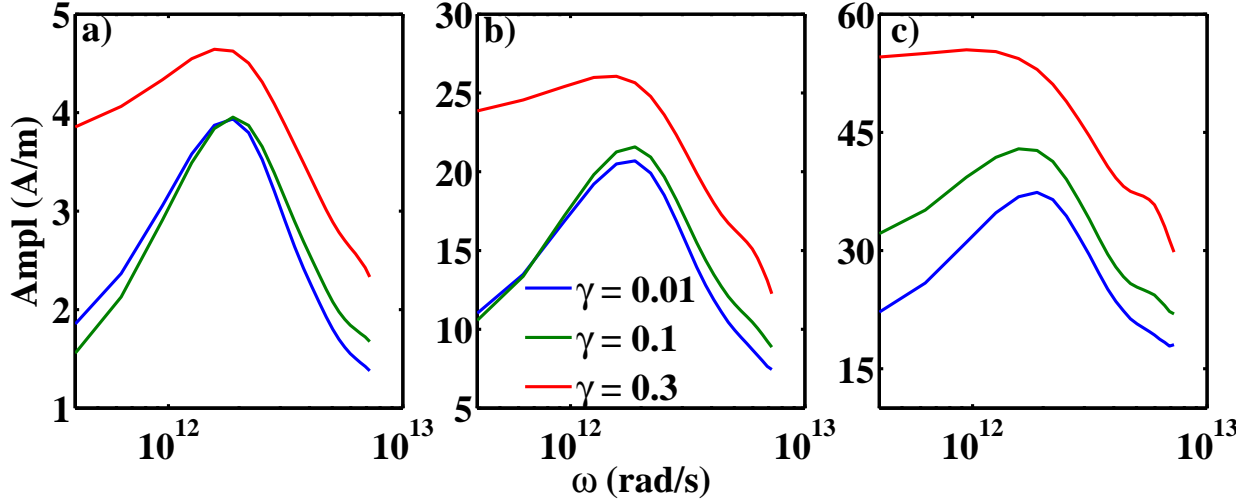
Figure 3.3: (Color online) Current density amplitude vs frequency for three different values of the damping parameter γ. (a) $F_1/F_o = 0.1$; (b) $F_1/F_o = 0.5$; (c) $F_1/F_o = 0.8$.

unexpected result is due to the fact that electrons take about $\tau_F \sim \hbar k_c/eF$ to reach the OP energy, and an additional τ_F to lose their energy once they reach the OP energy, as they can still accelerate before losing their energy. Consequently, the oscillation period is about $2\tau_F$ and $\omega_{resonance} \sim \omega_F/2$, which is the same as the current oscillations arising during the transient in the presence of the dc field F_o alone.[64,71] This anomalous value is due to the fact that the modulation of the ac field acts only upon the first half of the natural period, i.e., when carriers are field driven toward the OP energy, while the second half of the period when OP's are emitted is stochastic with a more complicated dependence on the field [see Eq. (3.3)], which is why the PR frequency is not exactly half of the natural frequency ω_F. From the figure, the oscillation amplitudes increase with γ, which as explained in Fig. 3.2 is due to increased scattering at low energy, sending back electrons close to the $\mathbf{k} = 0$ region, thereby further reducing the minimum values of the current density. The maximum values of the current density are not as affected because a substantial population of electrons is still able to reach high energies, even at high γ. Also, it is seen from the plots that the amplitude increases with F_1/F_o, as expected, since the difference between current density maxima and minima increases with F_1/F_o. Even though PR is achieved, it is rather "soft" because of the strongly dissipative nature of the back-and-forth motion of charge carriers in the constant field followed by OP emission. Obviously, this effect is more pronounced for the higher values of γ (low-energy scattering) and F_1/F_o (OP scattering) seen in the figure.

Figure 3.4 shows normalized current densities and electric fields versus time for different values of the parameters ω/ω_F and γ at low electric fields ($F_1/F_o = 0.1$, left column), and high fields ($F_1/F_o = 0.8$, right column). At low fields, the current is sinusoidal as expected from the linear response to the field. It is also observed that at very low frequencies ($\omega/\omega_F = 0.001$) and in the quasiballistic regime ($\gamma = 0.01$,
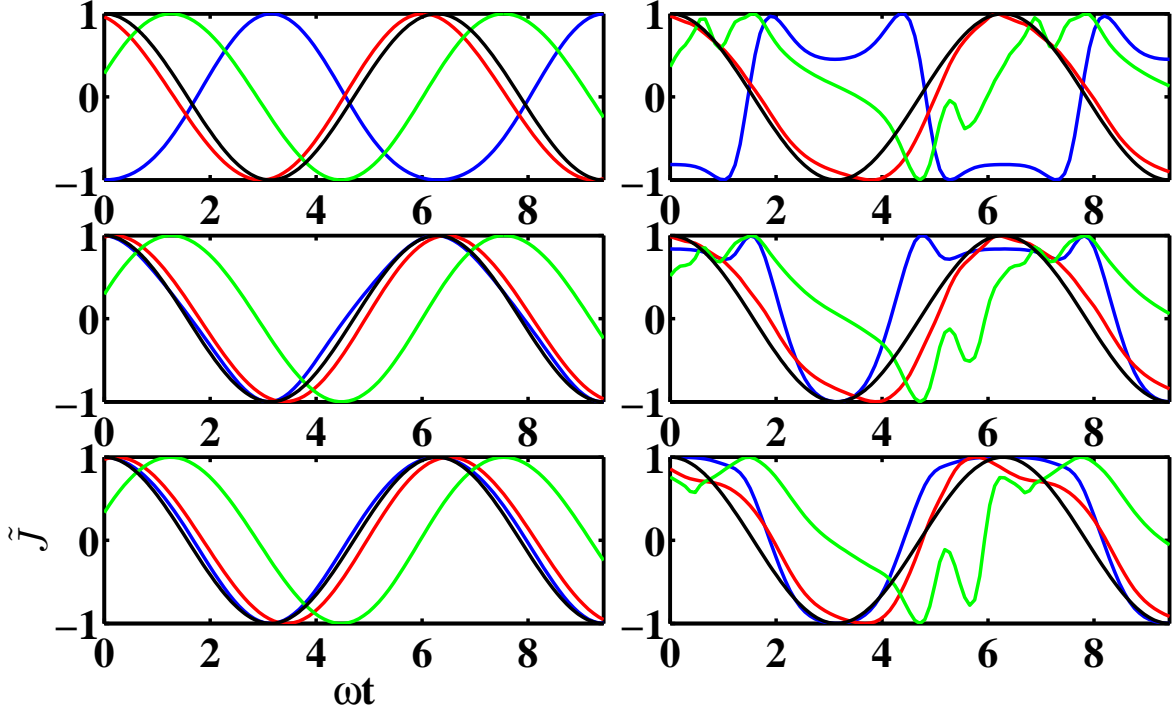
Figure 3.4: (Color online) Normalized values of the oscillating part of the current density vs time. Left column, $F_1/F_o = 0.1$; right column $F_1/F_o = 0.8$. Top row: $\gamma = 0.01$; middle row: $\gamma = 0.1$; and bottom row: $\gamma = 0.3$. Blue curve: $\omega/\omega_F = 0.001$; red curve: $\omega/\omega_F \approx 0.56$; green curve: $\omega/\omega_F = 2.3$; and black curve: normalized ac field.
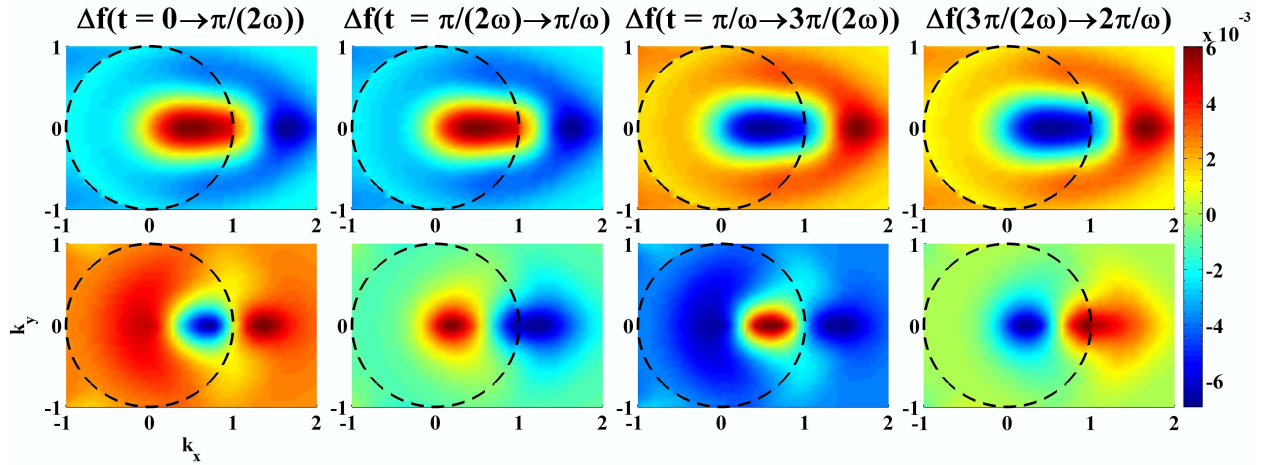
Figure 3.5: (Color online) 2D color plot of the electron distribution function difference Δf (as defined in the text, and normalized to the carriers density) in k space (normalized units of k/k_c) at four different times for field ratio $F_1/F_o = 0.1$ and damping $\gamma = 0.01$. Dashed circles correspond to the boundary $k = k_c$ between the low- and high-energy regions. Top row: $\omega/\omega_F = 0.001$. Bottom row: $\omega/\omega_F = 0.56$.

30

top left column), the current density is 180° out of phase with the field. In this case, as the field slowly decreases from $t = 0$ to $t = \pi/\omega$, the electronic system evolves adiabatically from a regime in high fields to that in low fields, which depletes the charge carriers in the high-energy region ($k > k_c$) and increases their concentration in the low-energy region ($k < k_c$). The current increases as the number of electrons with high k_x values ($k_c/2 < k_x < k_c$) in the low-energy region increases as a result of quasiballistic transport that results in a streamed DF. This situation is clearly seen in Fig. 3.5 (top row, first two panels), which shows the change in the DF with time $\Delta f = f[\omega t = (n+1)\pi/2] - f[\omega t = n\pi/2]$. From $t = \pi/\omega$ to $t = 2\pi/\omega$, the current decreases as the field increases because the electrons that penetrate deep into the high-energy region ($k > k_c$) with $k_x \gg k_y$ are scattered by OP emission equally to all $k' = k - \omega/v_F$ values. Indeed, the absence of q (phonon wave-vector) dependence in the deformation potential OP matrix element contributes to randomizing the DF,[50] specifically populating low-energy $\mathbf{k}$ states away from the field direction. This effect results in lowering the current (Fig. 3.5, top row, last two panels). In Fig. 3.4 (left column, top), it is seen that the phase between the current and the field reaches a minimum for frequencies approaching resonance ($\omega/\omega_F = 0.56$). This effect is better understood as the field increases from $t = \pi/\omega$ to $t = 3\pi/2\omega$, then to $t = 2\pi/\omega$, when the ac and the dc fields combine to enhance the back-and-forth motion of carriers between the low-energy $\mathbf{k}$ states (Fig. 3.5, bottom row, third panel) and the high-energy $\mathbf{k}$ states (fourth panel and first panel). For frequencies higher than resonance ($\omega/\omega_F \gg 0.56$), the dephasing between current and electric field starts to increase again (Fig. 3.6).

One also observes that as low-energy damping increases ($\gamma = 0.1$ and $\gamma = 0.3$; Fig. 3.4, left column), the dephasing between the current and the field at frequencies below resonance decreases (Fig. 3.6), as low-energy collisions result in diffusive transport that scatter electrons with high k_x states, thereby changing the streamed DF into a wider (k_y states) DF with lower current density. At intermediate damping ($\gamma = 0.1$), there is even a slight maximum before resonance, but above resonance the dephasing increases monotonically for all damping.

In higher ac fields (Fig. 3.4, right column), aside from the fact that the current curves are distorted by transport nonlinearity caused by competition between the dc and ac fields, the results concerning the phase difference between the oscillating F_1 field and the current densities are qualitatively the same. One notices, however, that the distortions do not affect the current at resonance, which remains quasisinusoidal. The effect of γ on the current density phase is also seen in Fig. 3.6. As expected, current density lags behind the electric field before resonance, but the dephasing also drops around resonance for low damping.
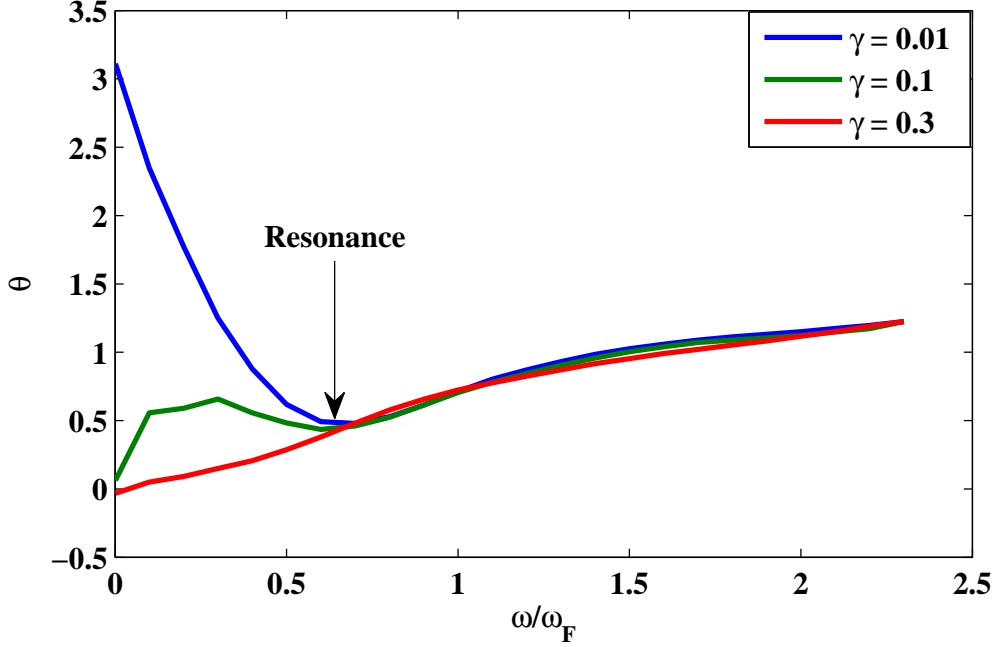
Figure 3.6: (Color online) Phase of the current density [compared to $F(t)$] for different values of the damping γ and field ratio $F_1/F_o = 0.1$.

3.4 CONCLUSIONS

Although this analysis is performed for time-dependent ac fields in the condition of spatial uniformity, it is also valid in the inverse condition of long-range periodically (oscillatory) modulated potential $V(x) = V(x+d)$ in the steady state. This can be seen from Eqs. (3.1), where the time-dependent differential $\partial/\partial t$ operator of the BTE LHS is replaced by the spatially varying $v_F \cos\phi\, \partial/\partial x$ operator, for which $\phi \sim 0$ in streamed DFs. Therefore, by making the substitution $t \to x/v_F$ in the formalism, the resonance condition between the periodic potential and the hot-carrier dynamics will arise for $F_o = (\hbar\omega_{OP})/0.56ed$ in the presence of an external field F_o, which could be used as field detector.

Let us notice that for carrier oscillations to occur in graphene, the electric field has to be high enough to escape low-energy scattering agents, but not too high as to overshoot the OP energy.[64] Also, at high damping, more scattering occurs in the low-energy region and the resulting oscillations are promptly damped. This problem persists even with the addition of a high amplitude ac field, and hence the wider resonance peak at high γ in Fig. 3.3. As a result, clean graphene samples should be used with low values of F_1/F_o for this effect to be observed, and be the basis for novel device applications either as a THz source or detector.

Chapter 4

ELECTRICAL TUNABILITY OF SOFT PARAMETRIC RESONANCE BY HOT ELECTRONS IN GRAPHENE*

Recently, it has been suggested that the electron current may exhibit damped transient oscillations due to the sudden quasi-ballistic acceleration of electrons up to the optic phonon (OP) energy $\hbar\omega_{OP}$, and their subsequent relaxation by OP, when a DC electric field F_o is turned-on.[64] This effect would arise provided that low-energy scattering is weak and the field is not too high i.e. $F_o \sim 0.5\text{-}2$ kV/cm, yielding oscillation frequencies of the order of $\omega_F = eF_o v_F/\hbar\omega_{OP}$ in the terahertz range.[64] It was also found that when an ac field is superimposed to the dc field a resonance in the oscillations occurs when the frequency of the ac field $\omega = \eta\omega_F$ with $\eta = 0.56$ for a field $F_o = 1$ kV/cm. This anomalous effect was called soft parametric resonance (SPR) because the frequency of the natural oscillations is modulated by the ac field in a strongly dissipative electronic system.[68] Asides from its fundamental peculiarity where the SPR coefficient η is anomalously smaller than one, unlike in normal PR where it is exactly 2,[67] SPR offers some technological advantage, as ω_F is tunable with the DC field F_o. In this chapter an investigation the sensitivity the SPR coefficient η to the DC electric field and the temperature for possible applications in THz technology is provided. For this purpose, the linear response theory that is shown to be less tedious than the large signal analysis previous used to predict SPR, but is also in good agreement with it is used. This model not only shows a weak sensitivity of η to F_o and temperature, but also reveals a new, but smaller intensity resonance $\omega = \omega_F$, i.e., $\eta = 1$ at lower T.

Consider a system of electrons in the conduction band of graphene, under the influence of a spatially homogeneous and time dependent electric field $F(t)$.[64] The electric field is applied in the positive k_x direction and is of the form $F(t) = F_o + F_1 e^{i\omega t}$, where F_1 is the ac amplitude with $F_1 \ll F_o$. As in previous work,[64,68] define two regions i.e. a low (I), and the high (II) energy regions in the momentum space, separated by the critical momentum $k_c = \omega_{OP}/v_F$ (Refs. 64 and 44) corresponding to the electron energy $\hbar\omega_{OP} = \hbar v_F k_c$ above which electrons emit OP's, and scatter back to region I, where they undergo quasi-ballistic acceleration

---

*This chapter closely follows Samwel Sekwao, and Jean-Pierre Leburton, *Appl. Phys. Lett.* **103**, 143108 (2013).

and low energy scattering with acoustic phonon and impurities.

The relaxation time approximation is used to account for low energy scattering (e.g., impurities and A.P),[47,64] so the Boltzmann Transport Equation (BTE) in the two regions read,[64]

$$\frac{\partial f_I(\vec{k},t)}{\partial t} + \frac{eF(t)}{\hbar}\frac{\partial f_I(\vec{k},t)}{\partial k_x} = -\frac{f_I(\vec{k},t) - f_{FD}(\vec{k})}{\tau_{LE}} + \sum_{\vec{k}'} S_{OP}(\vec{k}',\vec{k})f_{II}(\vec{k}',t), \tag{4.1a}$$

$$\frac{\partial f_{II}(\vec{k},t)}{\partial t} + \frac{eF(t)}{\hbar}\frac{\partial f_{II}(\vec{k},t)}{\partial k_x} = -f_{II}(\vec{k},t)\sum_{\vec{k}'} S_{OP}(\vec{k},\vec{k}'), \tag{4.1b}$$

where $f_I(\vec{k},t)$ and $f_{II}(\vec{k},t)$ are the distribution functions in the low and high energy regions, respectively. The function $f_{FD}(\vec{k})$ is the Fermi-Dirac distribution function ($k_F > 0$), $S_{OP}(\vec{k},\vec{k}')$ is the OP transition rate between the states $\vec{k}$ and $\vec{k}'$, and τ_{LE} is the relaxation time.[64] As in previous work, OP absorption is neglected as $N_q \ll 1(k_{BT} \ll \hbar\omega_{OP})$. Since $F_o \ll F_1$, we look for solutions $f(\vec{k},t) = f^o(\vec{k}) + f^1(\vec{k})e^{i\omega t}$, where $f^o(\vec{k})$ is the steady state solution of Eq. (4.1) with the applied field F_o,[64] and $f^1(\vec{k}) \ll f^o(\vec{k})$. Substituting this expression into Eq. (4.1), and linearize the BTE we get the following equations for $f^1(\vec{k})$,

$$\frac{eF_o}{\hbar}\frac{\partial f_I^1(\vec{k})}{\partial k_x} + \left(\frac{1}{\tau_{LE}} + i\omega\right)f_I^1(\vec{k}) = -\frac{eF_1}{\hbar}\frac{\partial f_I^o(\vec{k})}{\partial k_x} + \sum_{\vec{k}'} S_{OP}(\vec{k}',\vec{k})f_{II}^1(\vec{k}'), \tag{4.2a}$$

$$\frac{eF_o}{\hbar}\frac{\partial f_{II}^1(\vec{k})}{\partial k_x} + \left(\sum_{\vec{k}'} S_{OP}(\vec{k},\vec{k}') + i\omega\right)f_{II}^1(\vec{k}) = -\frac{eF_1}{\hbar}\frac{\partial f_{II}^o(\vec{k})}{\partial k_x}, \tag{4.2b}$$

where $f_I^1(\vec{k})$ and $f_{II}^1(\vec{k})$ are the solutions $f^1(\vec{k})$ in the low and high energy regions, respectively. The functions $f_I^o(\vec{k})$ and $f_{II}^o(\vec{k})$ are the steady state distribution functions in the low and high energy regions, respectively. Equation (4.2b) is readily solved, and the solution $f_{II}^1(\vec{k})$ is then substituted into Eq. (4.2a) to solve for $f_I^1(\vec{k})$. The two solutions are then matched at the boundary $k = k_c$ to obtain a solution everywhere on the plane.[44,64,68] Then we compute the 2D current density on the plane given by

$$J_x(t) = -4ev_F\sum_{\vec{k}} \Re f(\vec{k},t)\cos(\phi), \tag{4.3}$$

where ϕ is the angle between $\vec{k}$ and the k_x axis, and $f(\vec{k},t)$ is the distribution functions in the two regions. In this analysis, the results are expressed in the normalized ac frequency, ω/ω_F, where $\omega_F = 2\pi/\tau_F$, and

$$\tau_F = \frac{\hbar\omega_{OP}}{eFv_F} \tag{4.4}$$

34

is the time taken by ballistic carriers to reach the OP energy $\hbar\omega_{OP}$ from the Dirac point. Also, a dimensionless damping parameter γ given by

$$\gamma = \frac{1}{\tau_{LE} \sum_{\vec{k}'} S_{OP}(\vec{k}, \vec{k}')|_{k=1.5k_c}} \tag{4.5}$$

is used to gauge the strength of scattering in the low energy region.[64,68] Fig. 4.1(a) shows plots of the steady
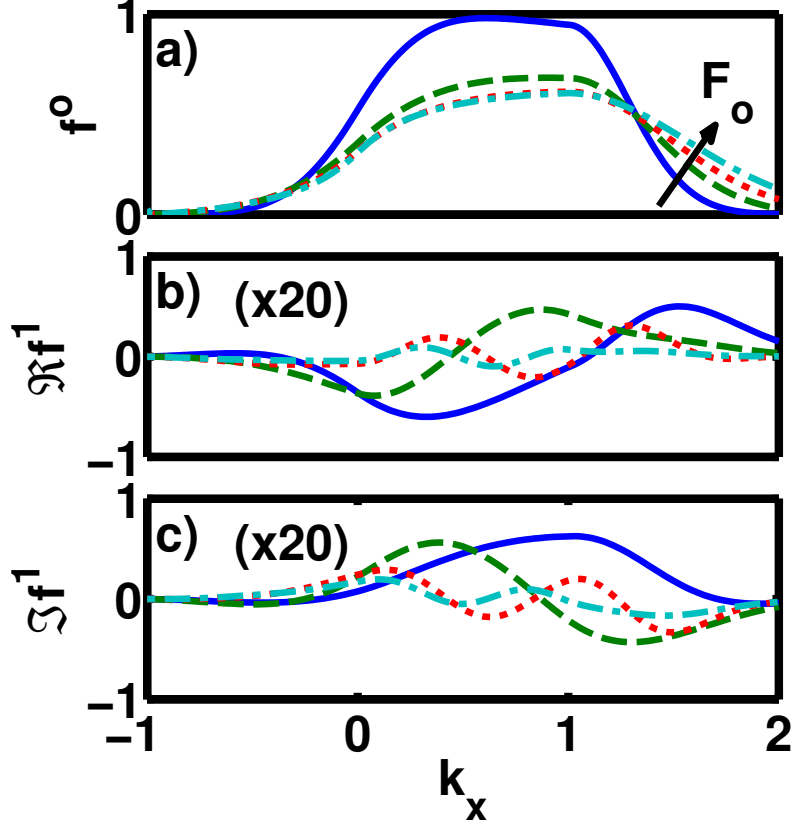

Figure 4.1: (Color online) (a) Cross-sections of the steady state distribution function f^o for different values of F_o. $\gamma = 0.01$. Solid lines ($F_o = 0.5$ kV/cm), dashed lines ($F_o = 1$ kV/cm), dotted lines ($F_o = 1.5$kV/cm), and dashed-dotted lines ($F_o = 2.0$ kV/cm). (b) Real part of the solution f^1 for different values of ω/ω_F. Solid lines ($\omega/\omega_F = 0.2$), dashed lines ($\omega/\omega_F = 0.54$), dotted lines ($\omega/\omega_F = 1.08$), and dashed-dotted lines ($\omega/\omega_F = 1.5$). $\gamma = 0.01$. (b) Imaginary part of the solution f^1 for different values of ω/ω_F. Solid lines ($\omega/\omega_F = 0.2$), dashed lines ($\omega/\omega_F = 0.54$), dotted lines ($\omega/\omega_F = 1.08$), and dashed-dotted lines ($\omega/\omega_F = 1.5$). $\gamma = 0.01$.

state distribution f^o along the k_x axis, for different values of the applied field F_o, and $\gamma = 0.01$. As seen from the figure, the concentration of carriers in region II increases as F_o increases. This is because carriers are more likely to penetrate deeper into the high energy region before they are scattered by OP's. Figures 4.1(b) and 4.1(c) show plots of the real and imaginary parts of the solution f^1 respectively, for different values of the applied frequency ω/ω_F, and $\gamma = 0.01$. One notices the real and imaginary parts of f^1 oscillates as a function of k_x with decreasing amplitudes as the applied frequency ω/ω_F increases.[68] We believe the origin of these oscillations resides in the coupling between time and k_x-momentum during the drift-motion of the

distribution in k-space, reflected in the "pseudo"-time invariance transformation $k'_x \Rightarrow k_x + \int_0^t F(s)ds$ of the differential terms of the BTE in Ref. 68
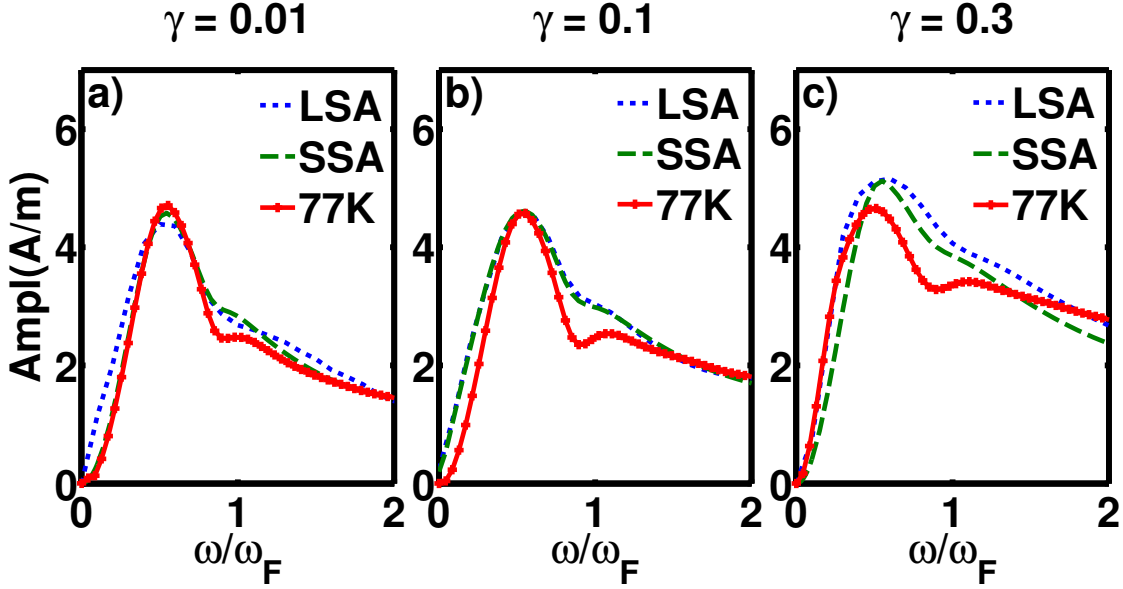

Figure 4.2: (Color online) Current density amplitude versus applied frequency for different values of γ. Comparing results from the Large Signal Analysis and the Small Signal Analysis at $T = 300$ K. Also shown SSA results at $T = 77$ K. $F_o = 1$ kV/cm, and $F_1/F_o = 0.1$. (a) $\gamma = 0.01$; (b) $\gamma = 0.1$; (c) $\gamma = 0.3$.

Fig. 4.2 shows a comparison of current density amplitude versus applied frequency results obtained by full solution of the BTE, and referred here as Large Signal Analysis (LSA), [68] and the linear solution obtained from Eq. (4.2), referred as the Small Signal Analysis (SSA), at $T = 300$ K. The figure also shows SSA results at $T = 77$ K. For both temperatures, the applied field is $F_o = 1$ kV/cm, and $F_1/F_o = 0.1$. From the figure, one can see that the two methods (LSA &SSA) give virtually the same results for the γ-values considered, as the two curves are on top of one another, thereby confirming the validity of the linear approximation for $F_1/F_o = 0.1$. One notices the SPR at $T = 77$ K persists at $\omega/\omega_F \approx 0.56$, [68] but is a little narrower than at $T = 300$ K, while a secondary peak is developing at $\omega/\omega_F \approx 1$. This second peak is due to the resonance of carriers oscillating between the Dirac point and the OP energy $\hbar\omega_{OP}$ for which the frequency is given by ω_F. At low temperatures, the carrier distribution function is narrower, which makes carrier acceleration toward OP more coherent. One notices however, that this second resonance does not involve the time spent by electrons to emit OP's at high energy, but only the acceleration toward OP energy. In fact, it is also present as a weak shoulder at $T = 300$ K, but is revealed at $T = 77$ K as the SPR sharpens due to the narrower distribution. Note that the LSA and SSA results at $T = 300$ K are obtained for frequencies in the range $0.1 \leq \omega/\omega_F \leq 2$, while SSA results at $T = 77$ K are for the frequencies $0 \leq \omega/\omega_F \leq 2$.

Fig. 4.3 shows the SSA current density amplitude versus applied frequency for different F_o values at
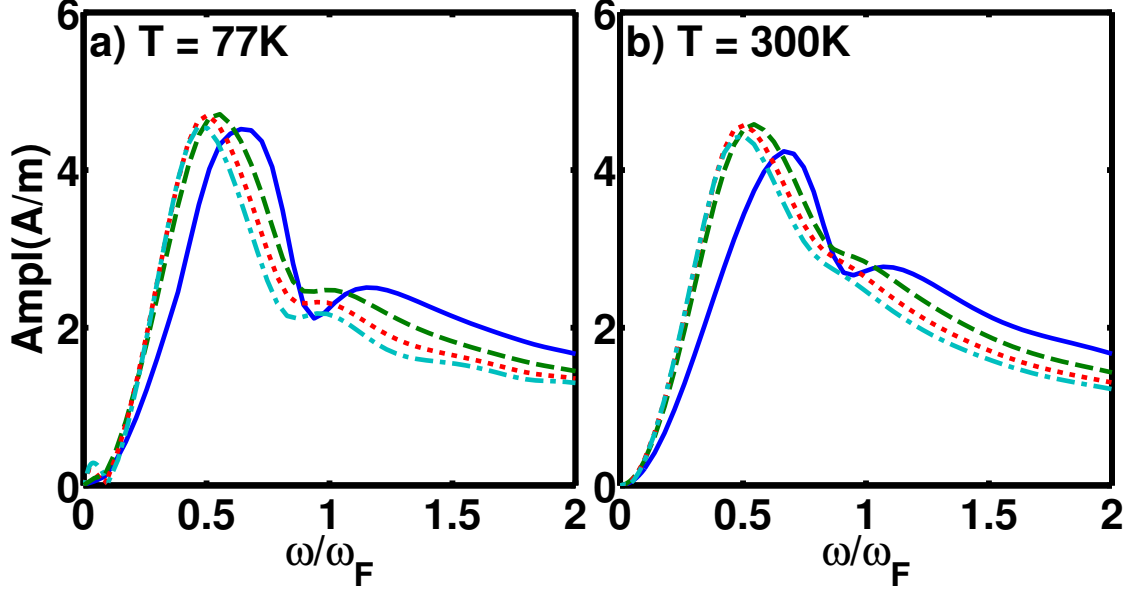
Figure 4.3: (Color online) Current density amplitude vs applied frequency for different values of F_o. (a) $T = 77$ K. (b) $T = 300$ K. $F_1/F_o = 0.1$, and $\gamma = 0.01$. Solid line ($F_o = 0.5$ kV/cm), dashed lines ($F_o = 1$ kV/cm), dotted lines ($F_o = 1.5$ kV/cm), and dashed-dotted lines ($F_o = 2$ kV/cm).

$T = 77$ K and $T = 300$ K, and for $F_1/F_o = 0.1$, and $\gamma = 0.01$. For both temperatures the SPR peak shift slightly to lower frequency, passing by a small maximum at $F_o = 1$ kV/cm as F_o increases, thereby indicating that the η parameter is a weak function of the DC field, as discussed in Fig. 4.4. Also for both temperatures, the second resonance peak, while following the same trend than the SPR peak is more prominent at low field.

In Figure 4.4, left axis, it is shown the variation of both resonance frequencies versus applied DC fields for both temperatures for which both resonance peaks remain practically unchanged. It can be seen that the SPR frequency (η parameter) decreases with the applied F_o field for both temperatures . As shown in a previous work,[68] SPR is achieved when the applied frequency ω is close to the actual frequency of damped oscillations of the carrier distribution during the transient turn-on of the DC field.[68] The actual period t^* of these oscillations consists of the quasi-ballistic carrier acceleration in the low energy region, τ_F, and the time spent in the high-energy region before emitting OP's. As seen from Fig. 4.1(a), as F_o increases, electrons are likely to spend more time in the high energy region, before OP emission occurs, and the period t^*/τ_F also increases.[64] As a result, one expects the resulting SPR frequency to decrease with F_o. However this variation of the parameter is relatively weak as seen in Figures 4.3 and 4.4, which is important for the SPR applications in terahertz technology, since it indicates that the SPR frequencies are tunable with F_o at both, low and room temperatures. The right axis of Fig. 4.4 shows the second resonant frequency ω_2 versus applied fields, which is practically constant at $\omega_2/\omega_F = 1$, except at very low fields, where it exceeds ω_F.
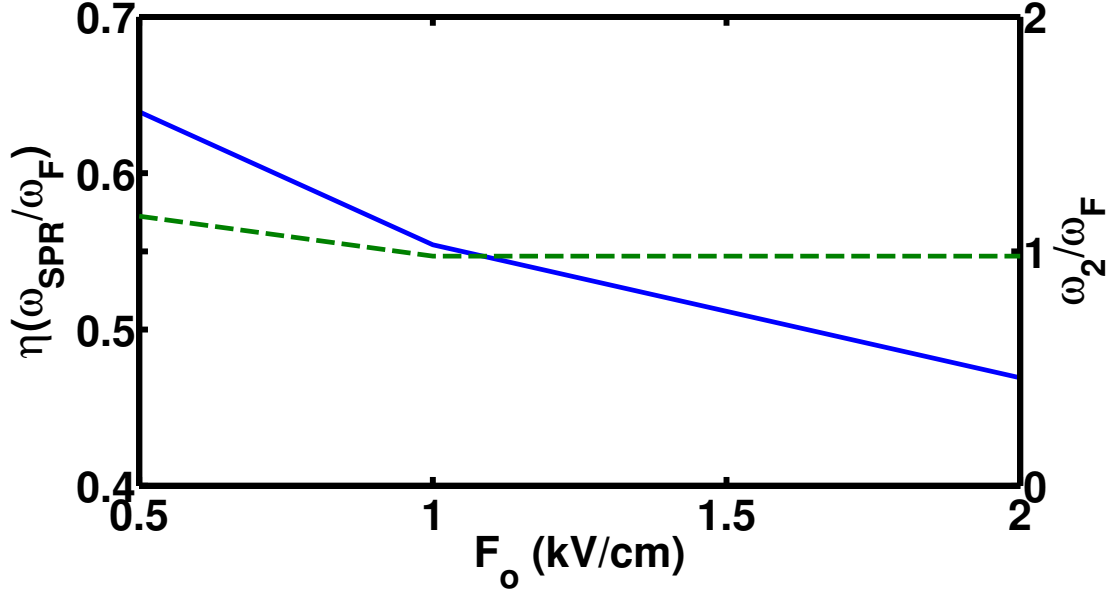
Figure 4.4: (Color online) Resonant frequency versus applied field for both $T = 77$ K, and $T = 300$ K. Left axis: First peak (solid). Right axis: Second peak (dash). $\gamma = 0.01$.

Figure 4.5 displays current density versus applied frequency for different values of γ, at $F_o = 0.5$ kV/cm for both temperatures. In both figures peaks are sharper at $T = 77$ K than at $T = 300$ K, and as γ increases, the first resonance peak shifts to lower values of ω_{SPR}/ω_F, as stronger low energy scattering delays the carrier distribution in reaching the high energy region to emit OP's, thereby decreasing the resonant frequency ω_{SPR}/ω_F, as already explained in Ref. 68. As in Figs. 4.2 and 4.3, the second resonance peak is also more pronounced at $T = 77$ K than at $T = 300$ K. However, unlike the SPR peak, the second resonance peak shifts to higher values of ω/ω_F as γ increases from 0.01 to 0.1.(Fig. 4.5(a),). Here too, strong scattering at low energy slows down carriers to reach the OP energy at a higher rate, thereby increasing ω/ω_F for resonance. The same effect is seen in Fig. 4.5(b) where the shoulder that identifies the second resonance shifts towards higher values of ω/ω_F as γ increases. At very high values of $\gamma(\gamma = 0.3)$, and both temperatures the oscillating current amplitudes increase, mainly due to the fact that during the low cycle of the amplitude the negative ac field reduces the overall field, which enhance the effect of low energy scattering as already observed in Ref. 68. In addition, carrier acceleration in the DC field F_o struggles to overcome low energy scattering, so the second resonance is less pronounced.

It has been shown that parametric resonance is achieved at different frequencies for different values of the applied dc field F_o, and ac fields with amplitude $F_1/F_o = 0.1$. The resonance is thus tunable with F_o at low and room temperatures. These results could have potential applications in terahertz technology. The emergence of a second resonance peak at low temperatures is also observed. This resonance peak is due to

38
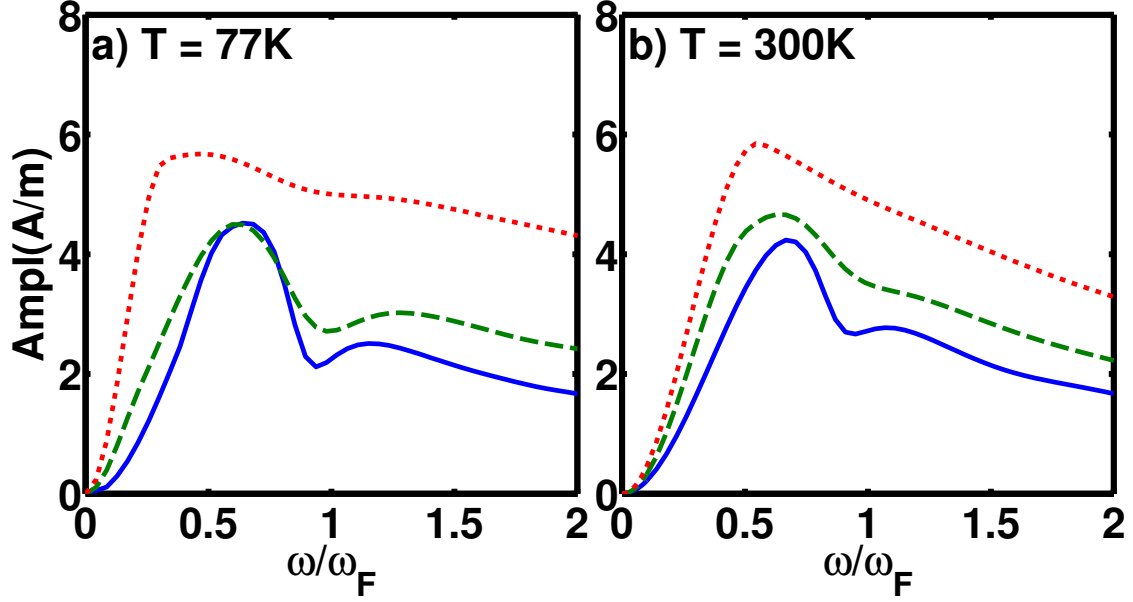
Figure 4.5: (Color online) Current density amplitude vs frequency for different values of γ. (a) $T = 77$ K and (b) $T = 300$ K. $F_1/F_o = 0.1$, and $F_o = 0.5$ kV/cm. Solid lines ($\gamma = 0.01$), dashed lines ($\gamma = 0.1$), and dotted lines ($\gamma = 0.3$).

the acceleration of carriers followed by OP relaxation at energy $\hbar\omega_{OP}$. If F_o is too high, the system may not reach resonance because of thermal broadening and or carriers escaping the high energy region without OP scattering. For best results, cleaner graphene samples should be used with the appropriate dc field.

Chapter 5

TERAHERTZ HARMONIC GENERATION IN GRAPHENE*

An interesting effect could arise if carriers in graphene are placed in periodic long range and time varying scattering to achieve transport resonance as well as possible frequency mixing. This kind of situation could be realized in free standing graphene sheets lying over periodically spaced narrow electric gates that would be regulated by an a-c field of appropriate frequency to modulate coulomb scattering of remote oxide impurities when carriers pass in front of the gates (Fig. 5.1). In the device, a DC field F_o is set up between the source S and the drain D, and the a-c field F_1 is applied between successive gates, so that charge carriers experience periodic electric fields and scattering times varying in time and distance along the channel.

In this chapter, it is shown that electronic current in graphene under the influence of time and space dependent periodic scattering and electric fields exhibits sharp resonances in the terahertz range, associated with the generation of higher harmonics characterized by large Q-factors tunable with scattering periodicity. The electron dynamics is investigated with a semi-classical Boltzmann formalism, where the effects of electron-electron interactions are ignored for low carrier concentrations ($n \ll 10^{12}/\text{cm}^2$).[27] Also, the electric fields considered in this study are not strong enough so that interband effects due to impact ionization[72] and tunneling[73] can be ignored.

As in the previous chapters, consider electrons in the conduction band of graphene in a field of the form $F(x,t) = F_o + F_1 e^{i(qx-\omega t)}$ with $0 < F_1/F_o < 1$, where F_o, and F_1 are the DC and a-c components respectively. The parameter q is the electric field wave number, and ω is the a-c frequency. In such fields, electrons accelerate until they gain enough energy to interact with OP's once $E \geq \hbar\omega_{OP}$, and suddenly lose their energy and momentum to re-accelerate quasi-ballistically in the fields, as this process repeats itself. In this dynamical picture, the momentum space can be divided into two regions I, and II that corresponds to electron energies $E < \hbar\omega_{OP}$, and $E \geq \hbar\omega_{OP}$ respectively. In region I, electrons accelerate while interacting with low energy scattering agents (AP's and impurities). In region II, the electrons interact with OP's and scatter back to region I. In low electron concentration ($n < 10^{12}/\text{cm}^2$), most of the electron population is stretched along the fields (streaming case), so that the majority of carriers have their velocity pointing in

---

*This chapter closely follows Samwel Sekwao, and Jean-Pierre Leburton, *Appl. Phys. Lett.* **106**, 063109 (2015).
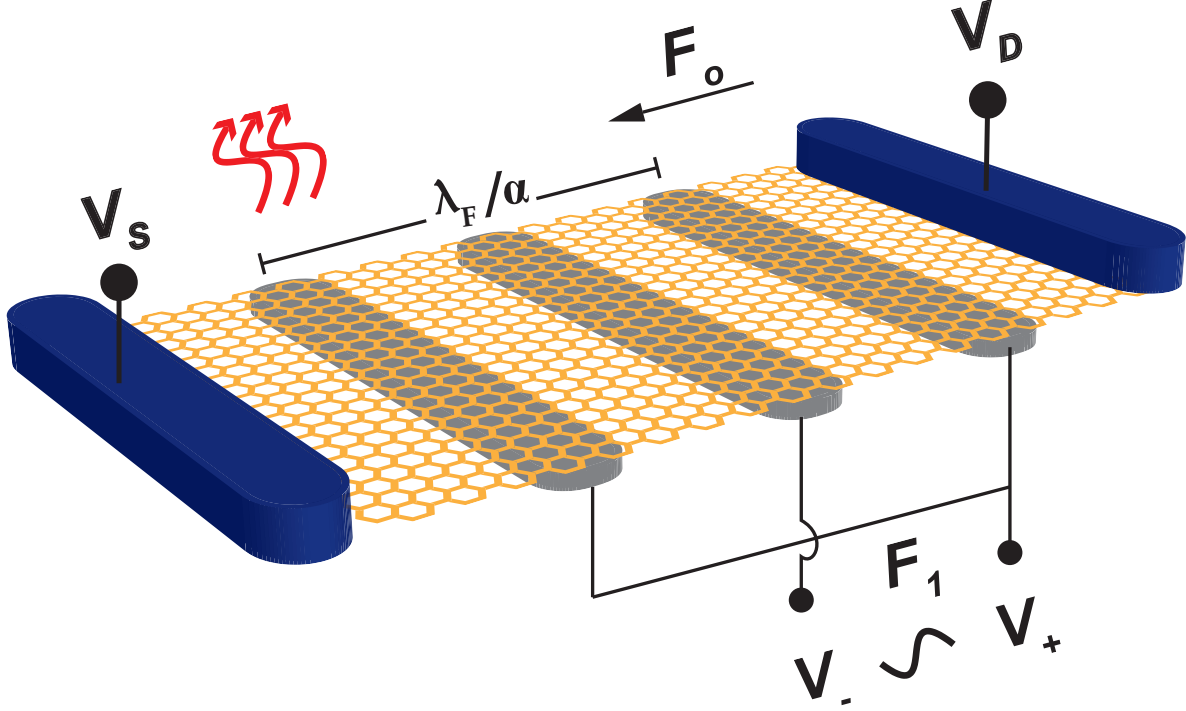
Figure 5.1: Color online) Schematics of a graphene based FET with periodic gating. The DC field F_o is applied between the source and the drain, and the AC field F_1 is applied between successive gates. The wavelength of the AC field is twice the distance between successive gates.

that direction.[64,73,74,75] If the fields are applied along the x- direction, the time and space dependent BTE in both regions reads

$$\frac{\partial f_I}{\partial t} + v_F \frac{\partial f_I}{\partial x} + \frac{eF(x,t)}{\hbar}\frac{\partial f_I}{\partial k_x} = -\frac{f_I - f_{FD}}{\tau(x,t)} + \sum_{\vec{k}'} S_{OP}(\vec{k}',\vec{k})f_{II}(\vec{k}',x,t) \tag{5.1a}$$

$$\frac{\partial f_{II}}{\partial t} + v_F \frac{\partial f_{II}}{\partial x} + \frac{eF(x,t)}{\hbar}\frac{\partial f_{II}}{\partial k_x} = -f_{II}\sum_{\vec{k}'} S_{OP}(\vec{k},\vec{k}') \tag{5.1b}$$

where f_I, and f_{II} are the distribution functions in regions I and II respectively, and f_{FD} is the Fermi-Dirac equilibrium distribution function ($k_F > 0$). Also, in the streaming case, one can assume $v_x \sim v_F$. Low energy elastic collisions in region I with impurities and AP's are accounted for within a local and time dependent relaxation time approximation[64] $\tau(x,t)$ with the same periodicity as the gate spacing and applied a-c field i.e.

$$\frac{1}{\tau(x,t)} = \frac{1}{\tau_o} + \frac{1}{\tau_1}e^{i(qx-\omega t)} \tag{5.2}$$

where τ_o is a constant relaxation time used to modulate the strength of low energy scattering (with impurities

and AP's), and τ_1 modulates scattering due to the periodic gates (see Fig 5.1). The expression $S_{OP}(\vec{k}, \vec{k}')$ is the OP transition rate between the states $\vec{k}$ and $\vec{k}'$ given by[52]

$$S_{OP}(\vec{k}, \vec{k}') = \frac{\pi D_o{}^2 (N_q + 1)(1 + \cos(\theta'))}{\sigma A \omega_{OP}} \delta(E' - E + \hbar\omega_{OP}) \tag{5.3}$$

where D_o is the optical deformation potential, N_q is the phonon occupation number, θ' is the angle between $\vec{k}$ and $\vec{k}'$, σ is the area density of the graphene sheet, and A is the area of the sheet. The effects of optic phonon absorption are neglected since their population is negligible, with $\hbar\omega_{OP} \gg k_B T$ even at room temperature. The second term on the Right Hand Side (RHS) of Eq. 5.1a is due to carriers repopulating region I after scattering with OP's, and the RHS of Eq. 5.1b is the corresponding depopulation term.

Due to the nature of the problem, a solution of the form

$$f(\vec{k}, x, t) = f^h(\vec{k}) + \sum_{m=-\infty}^{\infty} \sum_{n=-\infty}^{\infty} f^{mn}(\vec{k}) e^{i(mqx - n\omega t)} \tag{5.4}$$

is assumed, where $f^h(\vec{k}) = f^{00}$ is the solution to the homogeneous, steady state problem,[64] $f^{mn}(\vec{k})$ are the harmonic amplitudes, and the summation excludes all terms with $m = 0$ and $n = 0$, since they would result either in homogenous ($m = 0$) or state-state ($n = 0$) terms that are already taken into account in $f^h(\vec{k}) = f^{00}(\vec{k})$. Substituting Eq. 5.4 into Eq. 5.1, leads to the following recurrent equations for the individual harmonics;

$$\frac{eF_o}{\hbar} \frac{\partial f_I^{mn}}{\partial k_x} + \left[\frac{1}{\tau_o} + i(mqv_F - n\omega) \right] f_I^{mn} = -\frac{eF_1}{\hbar} \frac{\partial f_I^{(m-1)(n-1)}}{\partial k_x} - \frac{f_I^{(m-1)(n-1)}}{\tau_1}$$
$$+ \sum_{\vec{k}'} S_{OP}(\vec{k}', \vec{k}) f_{II}^{mn}(\vec{k}') \tag{5.5a}$$

$$\frac{eF_o}{\hbar} \frac{\partial f_{II}^{mn}}{\partial k_x} + \left[\sum_{\vec{k}'} S_{OP}(\vec{k}, \vec{k}') + i(mqv_F - n\omega) \right] f_{II}^{mn} = -\frac{eF_1}{\hbar} \frac{\partial f_{II}^{(m-1)(n-1)}}{\partial k_x} \tag{5.5b}$$

where f_I^{mn}, and f_{II}^{mn} are the harmonic amplitudes in regions I and II respectively. On setting $m = n = 0$ into Eq. 5.5, the terms in f^{00} satisfy the steady state, homogenous Boltzmann equation in the two regions, so that we get the following equations for $f^{-1,-1}$:

$$\frac{eF_1}{\hbar} \frac{\partial f_I^{-1,-1}}{\partial k_x} = -\frac{f_I^{-1,-1}}{\tau_1} \tag{5.6a}$$

$$\frac{eF_1}{\hbar} \frac{\partial f_{II}^{-1,-1}}{\partial k_x} = 0. \tag{5.6b}$$

Eq. 5.6b has the general solution $f_{II}^{-1,-1}(k_x, k_y) = g(k_y)$ which is unphysical, and should be set to zero, which by continuity in region I also yields $f_I^{-1,-1} = 0$. Because of the recurrence between f^{mn} and $f^{(m-1)(n-1)}$ in Eq. (5.5), we also have $f^{mm} = 0$ for all $m < -1$.

Let us now consider the harmonics f^{1n} with $n > 1$. Since the R.H.S of Eq 5.5b is zero, the solution for f_{II}^{1n} is readily obtained and reads

$$f_{II}^{1n} = f_b^{1n} \exp\left\{ -\frac{\hbar}{eF_o} \int_{k_x^o}^{k_x} \left[\sum_{\vec{k}'} S_{OP}(\vec{k}, \vec{k}')|_{k_x=z} + i(qv_F - n\omega) \right] dz \right\} \tag{5.7}$$

where the function f_b^{1n} is the solution f_{II}^{1n} evaluated at the boundary $k_x = k_x^o = \sqrt{(k_c)^2 - (k_y)^2}$. On substituting Eq. 5.7 into Eq. 5.5a, and evaluating the resulting equation at the boundary leads to a homogeneous integral equation of the form,

$$f_b^{1n}(k_y) = \int_{-k_x^o}^{k_x^o} dy f_b^{1n}(y) K(k_y, y, n), \tag{5.8}$$

where K is a complex kernel. Eq. 5.8 can be solved numerically by discretizing the integral,[76] which leads to a unitary matrix equation of the form $\tilde{K}\tilde{f} = \tilde{f}$. It is found that these eigenvectors exist only for $qv_F = n\omega$, which reduces Eq. 5.5 to the steady state-homogenous equation for $f^h = f_0^h$.[64] A similar analysis on the harmonics $f^{m1}, m > 1$ shows that solutions exist only, for $mqv_F = \omega$, so f^{m1} also reduces to f_0^h. Since f^{mn} are related to $f^{(m-1)(n-1)}$ by Eq. 5.5, it can be deduced from Eq. 5.5 that solutions for all the harmonics f^{mn} such that $m \neq n > 0$ that exist only when $\omega = mqv_F/n$, yield $f^{mn} = f_0^h$, and should therefore be discarded. As a result, only the harmonics f^{mn} such that $m, n > 0$ and $m = n > 0$ are the only remaining terms of the series (5.4) for $f(\vec{k}, x, t)$.

The current density on the plane is given by,

$$J_x(x, t) = -4ev_F \sum_{\vec{k}'} \Re f(\vec{k}', x, t) \cos(\phi') \tag{5.9}$$

where ϕ' is the angle between $\vec{k}'$ and the k_x' axis, and $\Re f(\vec{k}', x, t)$ is the real part of the distribution function. In this analysis, the a-c frequency is written in units of ω/ω_F, where $\omega_F = 2\pi eF_o v_F/\hbar\omega_{OP}$, and the
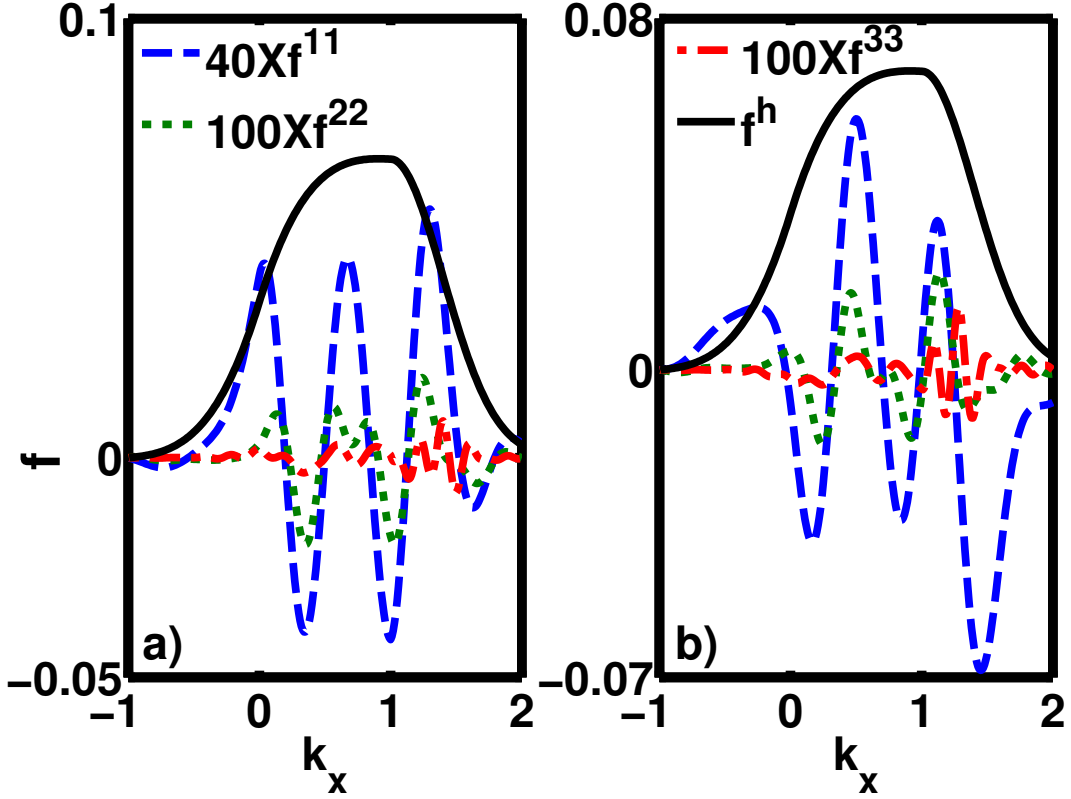
Figure 5.2: (Color online) (a) Cross-sections of real parts of the harmonics f^{11}, f^{22}, f^{33}, and homogeneous steady state distribution function f^h. (b)Imaginary parts and f^h. Dash ($40Xf^{11}$), dot ($100Xf^{22}$), dash-dot ($100Xf^{33}$), and solid (f^h). $F_o = 1$ kV/cm, $F_1/F_o = 0.1$, $\omega/\omega_F = 0.5$, $\tau_o/\tau_1 = 0.5$, and $\gamma = 0.01$.

wavelength is modulated by a dimensionless parameter α such that

$$q = \frac{2\pi\alpha}{\lambda_F}, \tag{5.10}$$

where $\lambda_F = \hbar\omega_{OP}/eF_o$, and $0 < \alpha \leq 1$. As in a previous work,[77] the dimensionless damping parameter γ given by

$$\gamma = \frac{1}{\tau_o \sum_{\vec{k}'} S_{OP}(\vec{k}, \vec{k}')|_{k=1.5k_c}} \tag{5.11}$$

is used to modulate the strength of low energy collisions compared to OP scattering.

Figure 5.2 shows cross sections of the real parts (5.2a), and imaginary parts (5.2b) of the first three harmonics f^{11}, f^{22}, f^{33}, with the steady state homogeneous distribution f^h along $k_y = 0$. The applied field in this case is $F_o = 1$kV/cm, such that $F_1/F_o = 0.1$, $\omega/\omega_F = 0.5$, and $\alpha = 1$. The low energy damping parameter is set at $\gamma = 0.01$, and $\tau_o/\tau_1 = 0.5$. From the figure, it can be seen that the harmonics oscillate as a function of k_x with amplitude f^{mm} decreasing as m increases, justifying the choice of the solution (5.4).
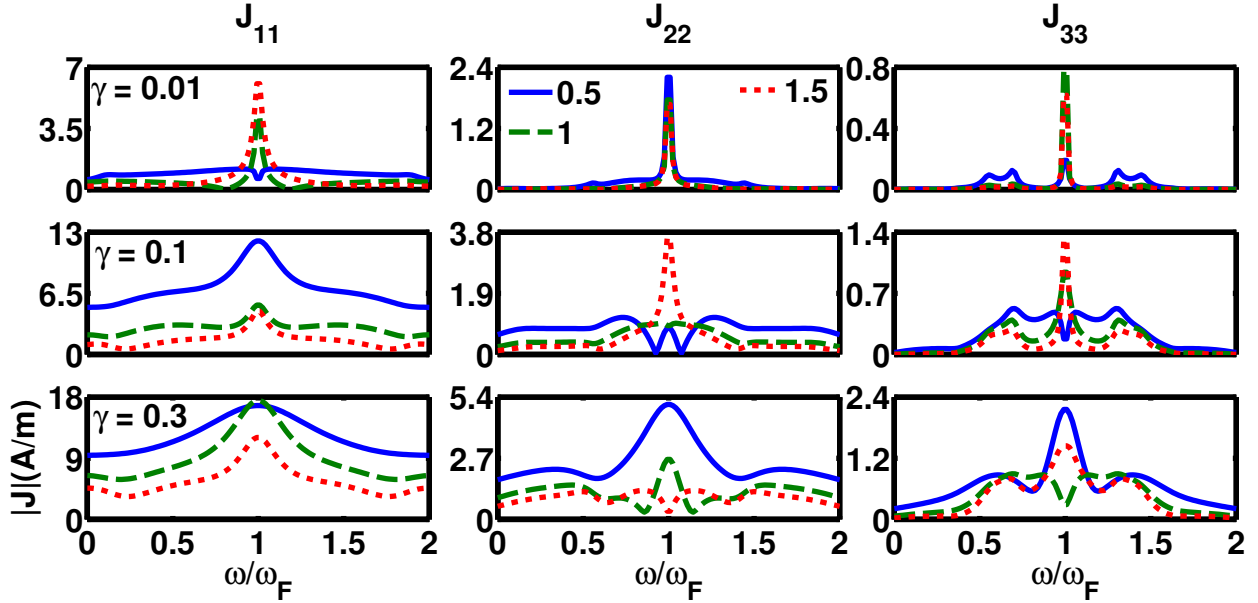
44

Also, note that f is always positive as $f^h \gg f^{mn}$.

Figure 5.3: (Color online) Current density amplitude versus frequency for different values of γ and F_o. (a) First harmonic. (b) Second harmonic. (c) Third harmonic. Top row ($\gamma = 0.01$), middle row ($\gamma = 0.1$), and bottom row ($\gamma = 0.3$). Solid ($F_o = 0.5$ kV/cm), dash ($F_o = 1$ kV/cm), and dot ($F_o = 1.5$ kV/cm). $F_1/F_o = 0.1$, $\tau_o/\tau_1 = 0.5$, and $\alpha = 1$.

Figure 5.3 displays the current density amplitude relative to the first three harmonics as a function of frequency for different values of F_o and γ. As in Fig. 5.2, the applied field is such that $F_1/F_o = 0.1$, $\tau_o/\tau_1 = 0.5$, and $\alpha = 1$. For all three harmonics, there are resonances that occur at $\omega = \omega_F$, for which the amplitudes $f^{mm}(k_x, k_y)$ are real, and the currents are in phase with the applied field. By considering the first row of Fig. 5.3 ($\gamma = 0.01$), one observes that there is no resonance for $F_o = 0.5$kV/cm (first column). This is because the contribution of the negative values of $f^{11}(k_x, k_y)$ in the total current (Eq. 5.9) offset that of the positive values at $\omega = \omega_F$. As the field increases from 0.5kV/cm to 1kV/cm, more electrons are able to escape low energy scattering in region I and reach the boundary $k = k_c$ and beyond, so the amplitude $f^{11}(k_x, k_y)$ increases in region II, inducing a net positive current, so as to achieve resonance. For all three harmonics, the resonance Quality factor, $Q = \omega_F/\Delta\omega_{FWHM}$, where $\Delta\omega_{FWHM}$ is the full width of the current density profile at half maximum value, first increases ($Q \approx 24.9$ to $Q \approx 25.2$ for the second, and $Q \approx 23$ to $Q \approx 28$ for the third) as the field increases from 0.5kV/cm to 1kV/cm. A further increase in the field to 1.5kV/cm causes more electrons to reach region II and scatter with OP's, broadening the distribution in the process. As a result, Q decreases (from $Q \approx 20$ to $Q \approx 13$ for the first harmonic, from $Q \approx 25.2$ to $Q \approx 24$ for the second, and from $Q \approx 28$ to $Q \approx 27$ for the third) as the field increase from 1kV/cm to 1.5kV/cm.

As low energy scattering (γ) increases, the system achieves resonance even at low fields (Fig. 5.3 first column). For the first harmonic, an increase in γ makes the amplitude more positive in region I, and the overall current becomes positive, achieving resonance. One can also see that the current density amplitude increases, while the overall resonance Q- factor decreases as low energy scattering increases. For the first harmonic with $\gamma = 0.1$ (second row, first column), one get $Q \approx 0.7$ ($F_o = 0.5\text{kV/cm}$), $Q \approx 0.7$ ($F_o = 1\text{kV/cm}$), and $Q \approx 6$ ($F_o = 1.5\text{kV/cm}$), only. This is due to the fact that low energy scattering redistribute carriers towards the $\vec{k} = 0$ region. As seen in a previous work,[68] carrier interactions with OP's are essential for resonance to occur. Higher γ-damping causes fewer carriers to interact with OP's and the resonance Q-factor decreases. The current density amplitude increases because the distribution increases around $\vec{k} = 0$. Note that when $\omega = \omega_F$, the system is a mixture of modes of oscillations with resonant frequencies $m\omega_F$.

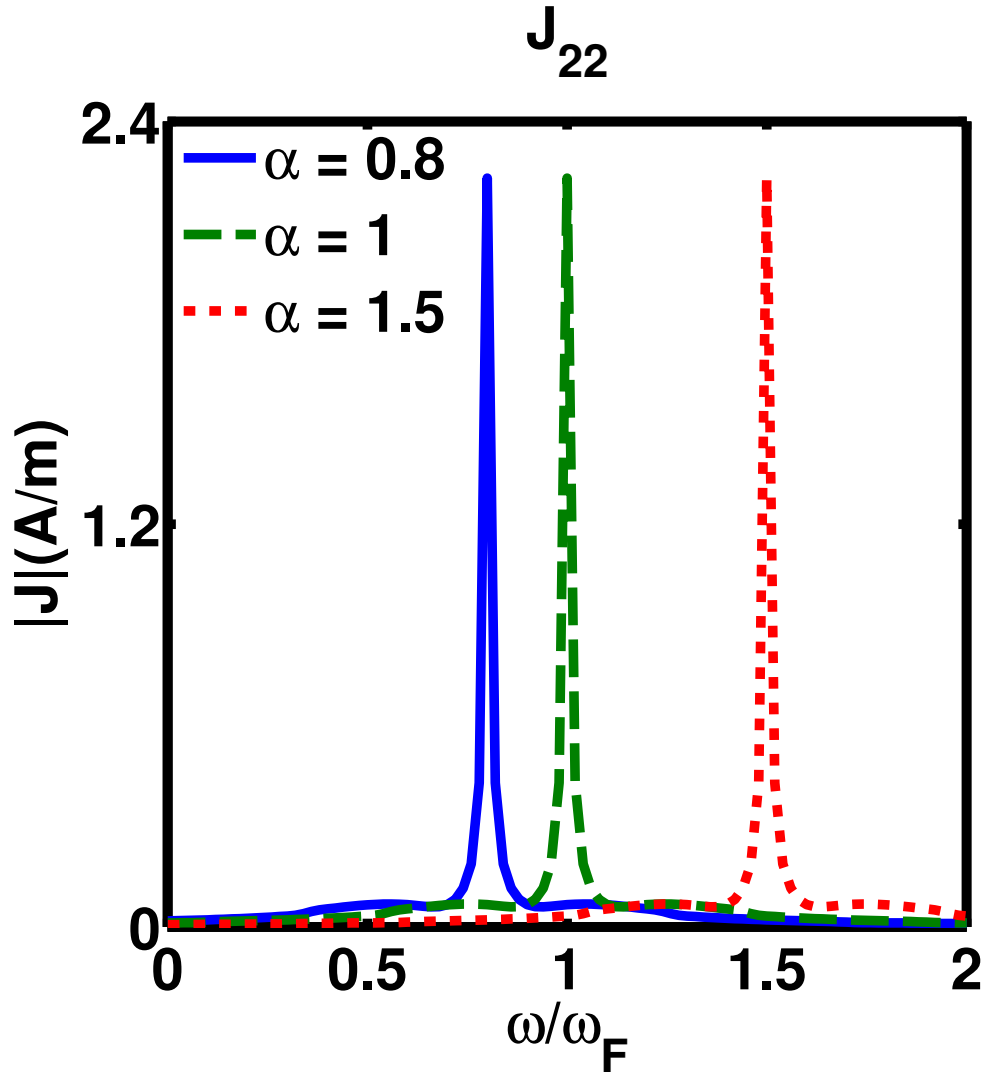**Figure 5.4:** (Color online) Second harmonic current density amplitude vs frequency for different values of α. Solid ($\alpha = 0.8$), dash ($\alpha = 1.0$) and dot ($\alpha = 1.5$). $F_1/F_o = 0.1$, $\tau_o/\tau_1 = 0.5$, and $\gamma = 0.01$.

Figure 5.4 shows plots of the second harmonic current density versus frequency for different values of α (gate spacing). The damping in this case is again set at $\gamma = 0.01$, $F_1/F_o = 0.1$, and $\tau_o/\tau_1 = 0.5$. From the figure, the observed resonances are achieved at the frequencies ω_F, $0.8\omega_F$, and $1.5\omega_F$ corresponding to $\alpha = 1$, $\alpha = 0.8$, and $\alpha = 1.5$ respectively, which shows that for a particular F_o, the resonance frequency is tunable with the wavelength of the applied field. This important result indicates the potential use of graphene in terahertz sources and detectors.[68,77]

In conclusion, an analysis of carrier dynamics in graphene subjected to periodic, time, and space dependent electric fields and scattering times has been carried out in this chapter. The model shows that, high Q resonances can be achieved when $\omega = \omega_F$. As expected, the Q-factors decrease with damping γ. Another observation is that at resonance, the system consists of carrier excitations with frequencies $m\omega_F$, for $m \geq 1$. As a result the system is essentially a mixer since an input frequency ω_F, creates the harmonics $m\omega_F$, and appropriate filters should be used to pick out the required frequencies. Also, the resonant frequency is tunable with the wavelength of the applied field. Note that the wavelength λ of the a-c field is twice the distance between successive gates in Fig. 5.1. Consequently, graphene can potentially be used to make high power, tunable terahertz devices that operate at room temperature.

Chapter 6

CONCLUSIONS

This dissertation presents a study of the dynamics of carriers in graphene under the influence of external electric fields. In particular, this dissertation analyses the interplay between the electric fields and OP scattering to generate current oscillations with frequencies in the THz range. Such oscillations had been predicted and observed in conventional semiconductors.[41,42] Room temperature observation of current oscillations in these materials is however not possible. This is because at room temperature, the OP energy $(\hbar\omega_{OP} \sim 0.04$ eV$)$[45] is comparable to thermal broadening of the charge distribution and the oscillations are immediately damped.[41,43,44] At low temperatures, impurity scattering becomes dominant and the oscillations are strongly damped. Impurity scattering can be reduced by lowering the dopant density which in turn lowers the carrier density reducing the oscillation amplitude in the process. The high values of conductivity and OP energy $(\hbar\omega_{OP} \sim 0.2$ eV$)$[38,39] of graphene make it possible for observing room temperature THz oscillations.

The onset of current oscillations in graphene is however restricted by low energy scattering. In device applications, charge impurity scattering can reduced by via screening. This cab be achieved by placing a graphene layer between two high K dielectrics.[57] Screening might however be offset by interface and remote static charges contained in the dielectrics.[58] Also, the presence of the substrate causes carriers in graphene to interact with remote interface phonons (RIP), increasing low energy scattering.[48,59,60,61] Freely suspended graphene layers should therefore be used for best results.

For carrier oscillations to occur in graphene, the applied field must be high enough that carriers escape low energy scattering and gain enough energy to interact with OP's. As a result, the process requires external biases V such that $V > \hbar\omega_{OP}/e$. The field should not be too high so that carriers are almost immediately scattered by OP's once they reach energies $E \geq \hbar\omega_{OP}$, so as to maintain coherence of the carrier distribution function. This condition is satisfied for $\tau_{gr} \gg \tau_{OP}$, which imposes an upper limit on the applied field, $F \ll 5$ kV/cm for $\tau_{OP} \approx 0.4$ ps. These conditions also require that sample lengths L such that $L > v_F\tau_{OP}$. Because the oscillations are damped after a few cycles, the sample length should not be higher than a few values of $\lambda = v_F\tau_{gr}$.

This dissertation also examines the effects of an additional spatially uniform ac field on the current oscillations in graphene. As discussed earlier, the frequency of the current oscillations depends on the applied dc field. The frequency of the ac component modulates the frequency of carrier oscillations, and the carriers behave as a parametric oscillator. Because of strongly dissipative nature of OP scattering, the system considered in this dissertation behaves differently to the usual parametric oscillators. Normal parametric resonance is achieved when the input frequency is twice the frequency of natural oscillations.[67] For the system of electrons in graphene, resonance is achieved for input frequencies ω such that $\omega = 0.56\omega_F$, where $\omega_F = 2\pi/\tau_{gr}$. When only the dc field is applied, the period of current oscillations is $t* \approx 1.8\tau_{gr}$. This is because, some electrons reach energies $E \geq \hbar\omega_{OP}$ and are not immediately scattered by OP's. These electrons penetrate deeper into the high energy region, stretching the period of the oscillations. As a result, the frequency of such oscillations is $0.56\omega_F$, thus resonance occurs when the input frequency matches the frequency of oscillations with just the dc field applied. The softness and anomaly of this type of parametric resonance can be attributed to the effectiveness of OP scattering of carriers in graphene. The same analysis can be applied to a system of electrons under the influence of a spatially dependent field that is periodically modulated, $F(x) = F(x + d)$, under steady state conditions,in the streaming case. The resonance condition in that case, $F_o = \hbar\omega_{OP}/0.56ed$, can be the basis of a field detector.

Based on the results of this dissertation, graphene may be used in THz devices that operate at room temperature. The imposed lower and upper limit on sample lengths ensure that such devices will be compact. The insensitivity of the resonance condition $\omega = \eta\omega_F$, $\eta \approx 0.56$, to the applied dc field F_o ensures that tunable resonant frequencies covering most of the THz range may be obtained. Sharper resonances at $\omega = \omega_F$ may be obtained in a graphene based FET with periodic gating. Harmonics with frequencies $m\omega_F$, $m > 1$ are also generated in this case. The fundamental frequency ω_F is also tunable with the gate separation. Consequently, high powered devices that create and detect electromagnetic radiation spanning the THz gap may be realized.

Appendix

Derivation of Equation 3.4

Boltzmann Transport Equation(BTE) in the two regions reads:

$$\frac{\partial f_L(\vec{k},t)}{\partial t} + \frac{eF(t)}{\hbar}\frac{\partial f_L(\vec{k},t)}{\partial k_x} = -\frac{f_L(\vec{k},t) - f_o(\vec{k})}{\tau_{LE}} + \sum_{\vec{k}'} S_{OP}(\vec{k}',\vec{k})f_H(\vec{k}',t) \tag{A.1a}$$

$$\frac{\partial f_H(\vec{k},t)}{\partial t} + \frac{eF(t)}{\hbar}\frac{\partial f_H(\vec{k},t)}{\partial k_x} = -f_H(\vec{k},t)\sum_{\vec{k}'} S_{OP}(\vec{k},\vec{k}') \tag{A.1b}$$

By using the substitution $\kappa = k_x + \beta(t)$, and choosing

$$\beta(t) = -\frac{e}{\hbar}\int_0^t F(s)ds, \tag{.2}$$

Eq. 1b reduces to

$$\frac{e}{\hbar}F(\beta^{-1}(\kappa - k_x))\frac{\partial g_H}{\partial k_x} = -g_H\sum_{\vec{k}'} S_{OP}(\vec{k},\vec{k}') \tag{.3}$$

where $g_H(k_x, k_y; \kappa) = f_H(k_x, k_y, \beta^{-1}(\kappa - k_x))$, and β^{-1} is the inverse function of β so that $\beta^{-1}\beta(t) = t$. The general solution of Eq. 3 above is of the form:

$$g_H(k_x, k_y; \kappa) = g_H(k_x^0, k_y; \kappa)\exp\left\{ -\frac{\hbar}{e}\int_{k_x^0}^{k_x} \frac{dp\,\tau_{OP}^{-1}(p, k_y)}{F[\beta^{-1}(\kappa - p)]} \right\}, \tag{.4}$$

where $k_x^0 = \sqrt{k_c^2 - k_y^2}$ is the k_x value at the boundary $k = k_c$, and

$$\tau_{OP}^{-1}(k_x, k_y) = \sum_{\vec{k}'} S_{OP}(\vec{k}, \vec{k}').$$

Using the substitution (2) above, the time dependent general solution of Eq. 1b is then

$$f_H(k_x, k_y, t) = f_b(k_y, \beta^{-1}(\beta(t) + k_x - k_x^0))M(k_x, k_y, t), \tag{.5}$$

50

where $f_b(k_y, t) = f_H(k_x^0, k_y, t)$ is the distribution function evaluated at the boundary, and

$$M(k_x, k_y, t) = \exp\left\{-\frac{\hbar}{e}\int_{k_x^0}^{k_x}\frac{dp\,\tau_{OP}^{-1}(p, k_y)}{F[\beta^{-1}(\beta(t) + k_x - p)]}\right\}.$$

The substitution (2) reduces Eq. 1a to;

$$\frac{\partial g_L}{\partial k_x} = \frac{\hbar}{eF(\beta^{-1}(\kappa - k_x))}\left\{-\frac{g_L - f_o}{\tau_{LE}} + \sum_{\vec{k}'} S_{OP}(\vec{k}', \vec{k})f_H(\vec{k}', \beta^{-1}(\kappa - k_x))\right\}. \tag{.6}$$

Eq. 6 is a first order partial differential equation with a solution of the form:

$$g_L(k_x, k_y; \kappa) = \frac{\hbar}{e}\exp\left\{-\frac{\beta^{-1}(\kappa - k_x)}{\tau_{LE}}\right\}\int_{-k_x^0}^{k_x}dp\frac{\left\{f_o(p, k_y) + \sum_{\vec{k}'}S_{OP}(\vec{k}', \vec{k})\Big|_{k_x=p}f_H(\vec{k}', t_1)\right\}\exp\left\{\frac{t_1}{\tau_{LE}}\right\}}{F(t_1)},$$

$$\tag{.7}$$

where $t_1 = \beta^{-1}(\kappa - p)$. Using Eq. 2, the time dependent solution of Eq. 1a is given by

$$f_L(k_x, k_y, t) = \frac{\hbar}{e}\exp\left\{-\frac{t}{\tau_{LE}}\right\}\int_{-k_x^0}^{k_x}dp\left\{f_o(p, k_y) + \sum_{\vec{k}'}S_{OP}(\vec{k}', \vec{k})\Big|_{k_x=p}f_H(\vec{k}', t_2)\right\}\exp\left\{\frac{t_2}{\tau_{LE}}\right\}/F(t_2), \tag{.8}$$

where $t_2 = \beta^{-1}(\beta(t) + k_x - p)$. On evaluating Eq. 8 at the boundary $k_x = k_x^0$, using the boundary condition $f_b(k_y, t) = f_L(k_x^0, k_y, t) = f_H(k_x^0, k_y, t)$, and Eq. 5 leads to an integral equation of the form:

$$f_b(k_y, t) = f_b^1(k_y, t) + \frac{\hbar}{2\pi^2 e}\int_{-k_x^0}^{k_x^0}dp\int d\vec{k}'S_{OP}(\vec{k}', \vec{k})\Big|_{k_x=p}f_b(k_y', t'')M(\vec{k}', t')\exp\left\{\frac{t'-t}{\tau_{LE}}\right\}/F(t'), \tag{.9}$$

where $\beta(t') = \beta(t) + k_x^0 - p$, $\beta(t'') = \beta(t') + k_x' - \sqrt{1 - (k_y')^2}$, $k_x' = k'\cos(\phi')$, $k_y' = k'\sin(\phi')$, and

$$f_b^1(k_y, t) = \frac{\hbar}{e}\int_{-k_x^0}^{k_x^0}dp\,f_o(p, k_y)\exp\left\{\frac{t'-t}{\tau_{LE}}\right\}/F(t'). \tag{.10}$$

References

[1] U. Welp, K. Kadowaki, and R. Kleiner, Nature Photonics **7**, 702 (2013).

[2] D. M. Mittleman, Nature Photonics **7**, 666 (2013).

[3] D. Abbot and X. C. Zhang, Proc. IEEE **95**, 1509 (2007).

[4] M. Tonouchi, Nature Photonics **1**, 97 (2007).

[5] B. Ferguson and X. C. Zhang, Nature Materials **1**, 26 (2006).

[6] T. Kleine-Ostmann and T. Nagatsuma, Journal of Infrared Millimeter and Terahertz waves **32**, 143 (2011).

[7] P. H. Siegel, IEEE Transactions on Microwave Theory and Techniques **52**, 24382447 (2004).

[8] T. Kampfrath, K. Tanaka, and K. A. Nelson, Nature Photonics **7**, 680 (2013).

[9] B. M. Williams, Nature Photonics **1**, 517 (2007).

[10] I. F. Akyildiz, J. M. Jornet, and C. Han, Physical Communication **12**, 16 (2014).

[11] P. Dean, A. Valavanis, J. Keeley, K. Bertling, Y. L. Lim, R. Alhathlool, A. D. Burnett, L. H. Li, S. P. Khanna, D. Indjin, et al., Journal of Physics D: Applied Physics **47**, 374008 (2014).

[12] A. Lee, Q. Qin, S. Kumar, and B. Williams, Applied Physics Letters **89**, 1411 (2006).

[13] P. Y. Ashish, S. D. Deepak, and E. B. Kiran, Drug Invention Today **5**, 157 (2013).

[14] P. H. Siegel, IEEE Transactions on Microwave Theory and Techniques **50**, 910 (2002).

[15] D. L. Woolard, E. R. Brown, M. Pepper, and M. Kemp, Proceedings of the IEEE **93**, 17221743 (2005).

[16] S. Kumar, IEEE Journal of Selected Topics in Quantum Electronics **17**, 38 (2011).

[17] M. Asada, S. Suzuki, and N. Kishimoto, Japan Journal of Applied Physics **47**, 43754384 (2008).

[18] S. Suzuki, M. Shiraishi, H. Shibayama, and M. Asada, IEEE Journal of Selected Topics in Quantum Electronics **19**, 8500108 (2013).

[19] C. Sirtori, S. Barbieri, and R. Colombelli, Nature Photonics **7**, 690 (2013).

[20] I. Focus, Nature Photonics **7**, 670 (2013).

[21] Q. Y. Lu, N. Bandyopadhyay, S. Slivken, Y. Bai, and M. Razeghi, Applied Physics Letters **103**, 011101 (20133).

[22] M. I. Katsnelson, Materials Today **10**, 20 (2007).

[23] P. R. Wallace, Physical Review **71**, 622 (1947).

[24] K. S. Novoselov, A. K. Geim, S. V. Morozov, D. Jiang, M. I. Katsnelson, I. V. Grigorieva, S. V. Dubonos, and A. A. Fristov, Nature (London) **438**, 197 (2005).

[25] R. E. Peierls, Ann. I. H. Poincare **5**, 177 (1935).

[26] L. D. Landau, Phys. Z. Sowjetunion **11**, 26 (1937).

[27] A. H. C. Neto, F. Guinea, N. M. R. Peres, K. S. Novoselov, and A. K. Geim, Review of Modern Physics **81**, 109 (2009).

[28] M. I. Katsnelson and K. S. Novoselov, Solid State Communicationa **143**, 3 (2007).

[29] S. A. Mikhailov, Europhysics Letters **79**, 27002 (2007).

[30] L. Liao, Nature **467**, 305 (2010).

[31] R. Saito, G. Dresselhaus, and M. S. Dresselhaus, *Physical Properties of Carbon Nanotubes* (Imperial College Press, 1998).

[32] S. Tiwari, *Compound Semiconductor Device Physics* (Academic Press, San Diego, CA, 1992).

[33] L. Britnell, R. V. Gorbachev, A. K. Geim, L. A. Ponomarenko, A. Mishchenko, M. T. Greenaway, T. M. Fromhold, K. S. Novoselov, and L. Eaves, Nature Communications **4**, 1794 (2013).

[34] O. Vafek, Physical Review Letters **97**, 266406 (2006).

[35] V. Ryzhii, A. Satou, and T. Otsuji, Journal of Applied Physics **101**, 024509 (2007).

[36] F. T. Vasko and V. Ryzhii, Physical Review B **77**, 195433 (2008).

[37] T. Jayasekera, B. D. Kong, K. W. Kim, and M. B. Nardelli, Physical Review Letters **104**, 146801 (2010).

[38] S. Piscanec, M. Lazzeri, F. Mauri, and A. Ferrari, Eur. Phys. J. Special Topics **148**, 159 (2007).

[39] A. C. Ferrari, J. C. Meyer, V. Scardaci, C. Casiraghi, M. Lazzeri, F. Mauri, S. Piscanec, D. Jiang, K. S. Novoselov, S. Roth, et al., Physical Review Letters **97**, 187401 (2006).

[40] W. Shockley, Bell System Technical Journal **30**, 990 (1951).

[41] A. Matulionis, J. Pozela, and A. Reklaitis, Physica Status Solidi (a) **31**, 83 (1975).

[42] H. Lochner, Journal of Applied Physics **43**, 3585 (1972).

[43] M. Brauer, Physica Status Solidi (b) **81**, 147 (1977).

[44] J. Leburton and R. Evrard, Journal of Low Temperature Physics **32**, 323 (1978).

[45] E. Kartheuser, *Polarons in Ionic Crystals and Polar Semiconductors* (American Elsevier, NATO Advanced Study Institute, Antwerp, 1971).

[46] W. A. Harrison, Physical Review **104**, 1281 (1956).

[47] Indeed, if for elastic deformation potential acoustic phonon, relaxation time approximation is legitimate, for ionized impurity scattering it is also reasonable within a momentum relaxation time expression, Karl Hess, Advanced Theory of Semiconductor Devices, p115. See also reference 22 in Barreiro et al, Phys. Rev. Lett. **103**. 076601 (2009).

[48] S. Fratini and F. Guinea, Physical Review B **77**, 195415 (2008).

[49] X. Du, I. Skachko, A. Barker, and E. Y. Andrei, Nature Nanotechnology **3**, 491 (2008).

[50] K. Hess, *Advanced Theory of Semiconductor Devices* (IEEE Press, 2000).

[51] S. Datta, *Quantum Phenomena* (Addison-Wesley, 1989).

[52] M. Lazzeri, S. Piscanec, F. Mauri, A. C. Ferrari, and J. Robertson, Physical Review Letters **95**, 236802 (2005).

[53] T. Fang, A. Konar, H. Xing, and D. Jena, Physical Review B **78**, 205403 (2008).

[54] J. T. Devreese and R. Evrard, Physica Status Solidi (b) **78**, 85 (1976).

[55] I. Meric, M. Y. Han, A. F. Young, B. Ozyilmaz, P. Kim, and K. L. Shepard, Nature Nanotechnology **3**, 654 (2008).

[56] J. B. Oostinga, H. B. Heersche, X. Liu, A. F. Morpurgo, and L. M. K. Vandersypen, Nature Materials **7**, 151 (2007).

[57] C. Jang, S. Adam, J.-H. Chen, E. D. Williams, S. D. Sarma, and M. S. Fuhrer, Physical Review Letters **101**, 146805 (2008).

[58] L. A. Ponomarenko, R. Yang, T. M. Mohiuddin, M. I. Katsnelson, K. S. Novoselov, S. V. Morozov, A. A. Zhukov, F. Schedin, E. W. Hill, and A. K. Geim, Physical Review Letters **102**, 206603 (2009).

[59] K. Hess and P. Vogl, Solid State Communications **30**, 807 (1979).

[60] J. Leburton and G. Dorda, Solid State Communications **40**, 1025 (1981).

[61] M. V. Fischetti, D. A. Neumayer, and E. A. Cartier, Journal of Applied Physics **90**, 4587 (2001).

[62] K. Bolotin, K. Sikes, Z. Jiang, M. Klima, G. Fudenberg, J. Hone, P. Kim, and H. Stormer, Solid State Communications **146**, 351 (2008).

[63] E. Fradkin, Physical Review B **33**, 3263 (1986).

[64] S. Sekwao and J.-P. Leburton, Physical Review B **83**, 075418 (2011).

[65] H. Kroemer., Solid-State Electronics **21**, 61 (1978).

[66] V. Perebeinos, J. Tersoff, and P. Avouris, Physical Review Letters **94**, 086802 (2005).

[67] F. Arscott, *Periodic Differential Equations* (Pergamon Press, 1964).

[68] S. Sekwao and J.-P. Leburton, Physical Review B **87**, 155424 (2013).

[69] This approximation does not affect the validity of our analysis as one can always apply it to bi-layer graphene where the band gap can be tailored so that $E_G > \hbar\omega_{op}$. See e.g. T. Ohta, A. Bostwick, T. Seyller, K. Horn and E. Rosenberg, Science 313, pp951-954 (2006).

[70] See Supplemental Material at [] for the complete derivation of equation (4).

[71] We note that in GaAs, the current oscillations period matches τ_F unlike in graphene. However, no PR study has been reported.

[72] A. Girdhar and J. P. Leburton, Applied Physics Letters **99**, 043107 (2011), erratum: 229903 (2011).

[73] I. I. Vosilius and I. B. Levinson, Soviet Physics Journal of Experimental and Theoretical Physics **23**, 1104 (1966).

[74] V. L. Kustov, V. I. Ryzhii, and Y. S. Sigov, Soviet Physics Journal of Experimental and Theoretical Physics **52**, 1207 (1980).

[75] Y. V. Gulyaev and I. I. Chusov, Soviet Physics Solid State **21**, 1362 (1979).

[76] A. J. Jerri, *Introduction to Integral Equations with Applications* (John Wiley and Sons, 1999).

[77] S. Sekwao and J.-P. Leburton, Applied Physics Letters **103**, 143108 (2013).